Università degli Studi di Roma "La Sapienza"

Facoltà di Ingegneria

DICEA - Dipartimento di Ingegneria Civile, Edile ed Ambientale
Area di Geodesia e Geomatica

Dottorato di Ricerca in Infrastrutture e Trasporti

PhD Thesis

A radargrammetric orientation model for SAR high resolution imagery

PhD Supervisor
Prof. Mattia Giovanni Crespi

PhD Student
Francesca Pieralice

A.A. 2009/2010

Contents

List of Figures

List of Tables

Chapter 1

Introduction

Today, imagery of our planet from spaceborne sensors are acquired continuously; a large number of satellite devoted to the Earth observation are available and also various kinds of sensors are on orbit.

As regards the Synthetic Aperture Radar (SAR) satellites for Earth observation, a possible geomatics application can be the generation of Digital Surface and Terrain Models (DSMs/DTMs).

DSMs and DTMs have large relevance in some territorial applications, such as topographic mapping, spatial and temporal change detection, feature extraction and data visualization.

DSMs extraction from satellite stereo pair offers some advantages, among which low cost, speed of data acquisition and processing, surveys of critical areas, easy monitoring of wide areas, availability of several commercial software and algorithms for data processing. In particular, the DSMs generation from SAR data offers the significant advantage of possible data acquisition during the night and in presence of clouds.

The availability of new high resolution SAR spaceborne sensors offers new interesting potentialities for the acquisition of data useful for the generation of DSMs. Two different approaches may be used to generate DSMs from SAR data: the interferometric and the radargrammetric one, both using a couple of images of the same area acquired from two different points of view.

The interferometry uses the phase differences information between the SAR images to lead the terrain elevation, unlike radargrammetric technique analyzes the signal amplitude and exploits the stereoscopy similarly to optical photogram-

metric methods. Actually, due to the low resolution amplitude supplied by the spaceborne radar sensors available until now (at the level of tens of meters), usually the first approach has been used, being aware that the radar interferometry may suffer for lack of coherence. At present, the importance of the radargrammetric approach is rapidly growing due to the new high resolution imagery (up to 1 m of ground resolution) which can be acquired by COSMO-SkyMed, TerraSAR-X and RADARSAT-2 sensors in SpotLight mode. In this sense, it seems useful to underline that the two approaches should be considered complementary, in order to obtain the best (accurate and complete) product.

The radargrammetric approach was first used in the 1950s; then, as mentioned, it was less and less used, due to the quite low resolution in amplitude of radar images, if compared to their high resolution in phase. Some researchers have investigated the DSMs generation from SAR data acquired by the various sensors available: several results about data acquired by lower resolution satellite, like RADARSAT-1 and ERS1/2, have been published by Toutin in [1] or [2]; quite recently, as regards the new-generation high resolution SAR satellite, the potentialities of TerraSAR-X [3] and Radarsat-2 [4] have been investigated by Raggam et al. and by Toutin and Chenier respectively.

DSM extraction procedure consists of two basic steps: the stereo pair orientation and the image matching for the automatic detection of homologous points. In this thesis the topics related to image orientation of SAR stereo pairs in zero-Doppler geometry acquired in SpotLight mode are investigated.

As regards the radargrammetric orientation model, it has to be underlined that, starting from the model proposed in the classical book of Leberl [5], a refinement of the orbital model have to be taken into account to comply with and to exploit the potentialities of the novel high resolution (both in azimuth and in range). Then, the defined and implemented model performs a 3D orientation based on two range and two zero-Doppler equations, allowing for the least squares estimation of some calibration parameters, related to satellite position and velocity.

The model has been implemented in SISAR (Software per Immagini Satellitari ad Alta Risoluzione), a scientific software developed at Geodesy and Geomatic Institute of the University of Rome "La Sapienza". This software was at first devoted to the orientation of high resolution optical imagery [6], and in the last year it has been extended also to SAR imagery.

Moreover a tool for the SAR Rational Polynomial Coefficients (RPCs) generation has been implemented in SISAR software, similarly to the one already developed for the optical sensors.

The Rational Polynomial Functions (RPFs) model with the employment of RPCs is a well known method to orientate optical satellite imagery. In fact, some satellite imagery vendors have considered the use of RPFs models as a

standard to supply a re-parametrized form of the rigorous sensor model in terms of the RPCs, that implicitly provide the interior and external sensor orientation. This generalized method is very simple, since its implementation is standard and unique for all the sensors; moreover the performances of the RPFs model using the RPCs can reach the level of the ones from rigorous models.

The possibility to generate RPCs starting from a rigorous model sounds of particular interest since, at present, the most part of SAR imagery is not supplied with RPCs, although the RPFs model is available in several commercial software. The RPCs can be an useful tool in place of the rigorous model in processes as the image orthorectification/geocoding or as the DSMs generation, since the RPFs model is very simple and fast to be applied.

Deeper investigations in the least squares RPCs estimation underlined that many RPCs are correlated; so, in our approach the Singular Value Decomposition (SVD) and QR decomposition are employed to evaluate the actual rank of the design matrix and to select the actual estimable coefficients, avoiding an overparametrization of the model.

It is well known that the optimum stereo imagery configuration for the radargrammetric application is when the target is observed in opposite-side view; however it causes large geometric and radiometric disparities, hindering the image matching, which is the second fundamental step for DSMs generation after the imagery orientation. A good compromise is to use a same-side configuration stereo pair with a convenient base to height ratio, in order to increase the efficiency in the correlation image process.

In this thesis the results of some tests performed on COSMO-SkyMed and TerraSAR-X SpotLight stereo pairs are presented; the data available are two COSMO-SkyMed same-side stereo pairs, acquired over the areas of Maussane (Southern France) and Merano (Northern Italy), and three TerraSAR-X images, acquired over the area of Hannover (Northern Germany), from which a same-side and an opposite-side stereo pairs have been derived.

The results concern the stereo orientation using both the radargrammetric and the RPCs model. The results are compared to those stemming from commercial software PCI Geomatica v. 10.3, where the well known Toutin's model is implemented.

Chapter 2

Satellite sensors for the remote sensing

Today, imagery of our planet from spaceborne sensors are acquired continuously; they have become powerful scientific tools to enable better understanding and improved management of the Earth and its environment.

Earth Observation imagery show the world through a wide-enough frame so that complete large-scale phenomena can be observed.

The short times of acquisition of information satisfy the demand for the monitoring of rapid changes in the ground and in anthropic activities; for this reason the studies about the remote sensing developed very fast in the last years.

2.1 Remote sensing spaceborne sensors for environmental and geomatics applications

At the present a large number of satellite devoted to the Earth observation are available and also various kinds of sensors are on orbit. These kind of sophisticated instruments provide continuous observation and monitoring of the Earth's land, atmosphere and oceans, and they are valid tools to provide a wealth of information on the workings of the Earth system, including insights into factors contributing to climate change.

The various sensors differ for working methods, types of measured characteristics, resolution and scale of monitoring.

If we just limit our considerations to remote sensing sensors optical and radar sensors with high resolution are suitable to achieve detailed information about the territory, for a large number of application, as environmental, monitoring engineering, geology, security, land planning and management of Earth's resources.

As regards SAR (Synthetic Aperture Radar) and optical satellites for Earth observation, the geomatics applications can be classified in four main categories: topographic mapping, deformation mapping, thematic mapping based on change detection, thematic mapping based on classification.

In particular, the optical High Resolution Satellite Imagery (HRSI) become important for cartographic purposes: for instance, they could be a suitable alternative to aerial photogrammetric data to update and produce maps at 1:5000 scale or lower, to produce orthophotomaps, or to generate Digital Surface and Terrain Models (DSM/DTM).

In addition to optical imagery, also SAR imagery are suitable for the DSM generation using radargrammetric or, more commonly, interferometric methods; to this aim, special mission have been set up, as the Shuttle Radar Topography Mission (SRTM), specially designed to yield elevation data on world scale, or ERS-1/2 tandem mission, or TanDEM-X mission in the last years.

The technique of differential InSAR (Interferometric SAR) can provide observation of ground motion and deformation mapping in many application fields, like seismic studies, volcano deformation monitoring, land subsidence, glacier and ice motion.

Thematic mapping can use both optical and SAR data, and a valid method could be represented by the change detection. For example, the changes in the scattering characteristics of the ground surface between two radar acquisition can result in a change of coherence in the interferogram; the analysis of the decrease of coherence can be associated with different types of land use.

As support to the thematic mapping, a large number of classification methods are existing; to this aim, optical imagery are well-suited, specially multispectral or hyperspectral imagery.

The remote sensing presents advantages in comparison with other kinds of survey thanks to the synoptic feature of information with multispectral and multitemporal data vision, together with high frequency of acquisition due to the short revisit time of spacecraft.

For example, in comparison with the classical aerial photogrammetric survey, the satellite remote sensing offers some advantages:

- easy monitoring of wide areas
- availability of digital and multispectral data

- survey at regular interval, depending only on satellite revisit time (variable from 1 day to few tens of days)
- survey of areas critical from the logistic point of view, where the organization of photogrammetric flights is difficult; this advantage is especially important for the medium scale cartography in developing countries or in countries with difficult political situations

First generation of satellite sensors (as Landsat 5 and 7, SPOT 4, IRS, ERS) were characterized by low spatial resolution that did not allow the acquisition of data for detailed studies. Thanks to the second generation satellites (as IKONOS, QuickBird, WorldView-1, GeoEye-1, Cosmo-SkyMED, TerraSAR-X), it is now possible to acquire imagery with geometric and semantic features suited for realization and update of technical map on medium scale (1:25000-1:10000) and possibly larger scale (up to 1:5000). In this section we are going to show the main features of these satellites and sensors.

2.2 Satellite orbit features

The target of satellite mission is to acquire the largest number of images with the best quality and the best areal coverage; in fact, the satellite orbit is determined by the combination of these requisites and by the revisit time and the distance Earth-satellite.

The orbit is planned considering the fact that the satellite has to observe the widest possible area of the Earth for a reasonable number of repetitions.

The preferred orbits for the Earth observation are usually Low Earth Orbits (LEO) with an altitude between 300 km and 1000 km. This choice represents a compromise between the necessity of a close observation of the Earth and the lifetime of the satellite; in fact the low orbit improves the resolution of images but produces negative effects such as atmospheric drag and gravitational perturbation which are the causes of the satellite lifetime reduction.

Also, the light condition, which is a crucial factor for the acquisition of optical imagery, is fundamental in the choice of the orbit.

The sun angle is the angle between the local zenith and the direction of sunbeam; it defines the light condition (Figure 2.1). The best light condition is obtained with a less sun angle (sun at zenith), but presence of little shades could help the observer to recognize details and for a better interpretation of image. For this reasons sun angle usually can changes from 20° to 40°.

To guarantee the same lighting at each satellite passage, a Sun-Synchronous Orbit (SSO) is used (Figure 2.2). In this orbit the angle between Earth-Sun direction and the orbit plane is constant and the satellite flies over a certain area at the same local time therefore under the same conditions of light. The weather

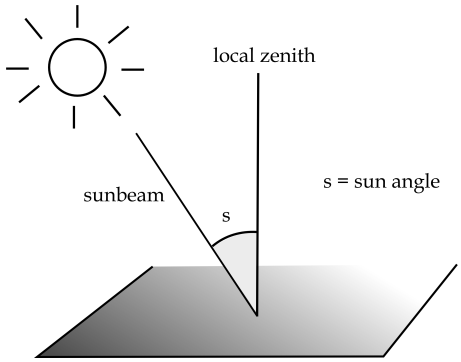

Figure 2.1: Sun angle

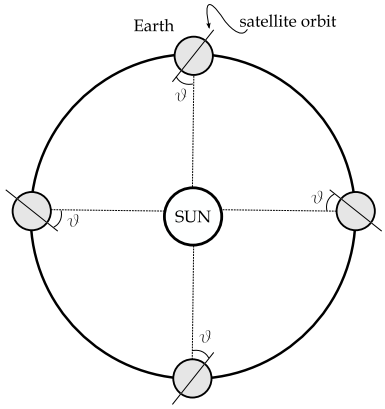

Figure 2.2: Sun-synchronous orbit

situations, such as mist, fog and clouds, are obviously unknown and are serious problem for the image acquisition. Obviously, this condition is important only in the case of optical images.

The inclination of the orbit - the angle between the orbital and the equatorial planes - is another relevant parameter to determine the satellite orbit (Figure 2.3). Orbits with large inclination - like pseudo-polar orbits - permit a total coverage of the Earth with only a very slight loss of data on the poles, whereas small inclinations are better in case of specific studies, for example on equatorial area. A good coverage depends not only on the orbit choice but also on the coverage of receiving stations, and on satellite revisit period.

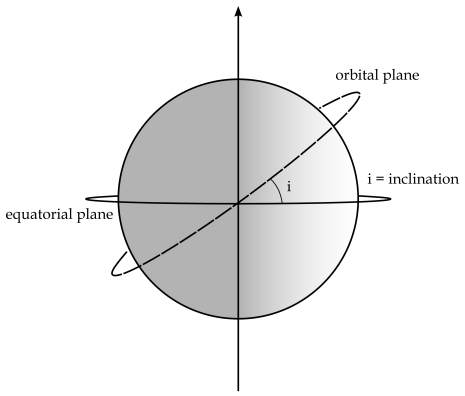

Figure 2.3: Orbit inclination

The revisit period is the time between two consecutive acquisitions of the same area; for a satellite sensor it is usually of several days. In order to guarantee very short revisit period, satellite constellations have been launched on orbit, as Cosmo-SkyMED, TerraSAR-X and TanDEM-X, or Pleiades.

Actually, the majority of satellites offer overlap between contiguous orbits and for this reason some areas of the Earth can be acquired more frequently.

Some satellites are able to orient their sensors to shoot the same area in different passages, with shorter time intervals. The revisit period depends also on the inclination of the orbit and it is shorter if the inclination is smaller: this is the main disadvantage of the polar orbits.

2.3 Sensor characteristics

In the following sections, the main characteristics of optical and radar sensors will be described.

2.3.1 Spectral resolution

The spectral resolution is the amplitude of the spectral bands (wavelength interval of the electromagnetic spectrum) that an optical sensor can distinguish or at which a radar sensor works (Figure 2.4 and Table 2.1).

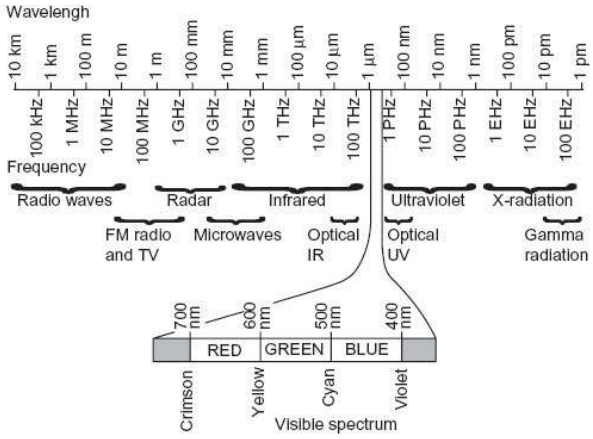

Figure 2.4: Electromagnetic spectrum

In particular the optical sensors are passive sensors, able to register the radiation that is reflected by the Earth's surface. Each sensor is characterized by the spectral bands in which it is sensible.

Radar sensors are active sensor, providing its own illumination in form of microwaves, and they are able to emit, receive and record the signal echoes reflected by the Earth's surface; also in this case each sensor is characterized by the spectral bands in which it works.

The spectral resolution depends on the kind of sensor, the optical satellite sensor usually acquires the image in panchromatic, multispectral or hyperspectral mode:

- panchromatic sensor is sensitive to all wavelengths of visible and near-infrared; the final image is in black and white
- multispectral sensor can distinguish different spectral bands in the visible and near infrared regions; an image is created for each individual wavelength interval
- hyperspectral sensor is an advanced multispectral sensor; it can detect hundreds of very narrow spectral bands throughout the visible, near-infrared and mid-infrared regions

Band	Frequency (GHz)	Wavelength (cm)
P	0.255-0.390	133.0-76.9
L	0.390-1.550	76.9-19.3
S	1.550-4.20	19.3-7.1
C	4.20-5.75	7.1-5.2
X	5.750-10.90	5.2-2.7
K	10.90-36.0	2.7-0.83
K_u	10.90-22.0	2.7-1.36
K_a	22.0-36.0	1.36-0.83
Q	36.0-46.0	0.83-0.65
V	46.0-56.0	0.65-0.53
W	56.0-100.0	0.53-0.30

Table 2.1: Bands of the microwave region

Studies point out that the best sensors for cartographic applications are the panchromatic ones. Panchromatic sensors present a spatial resolution about four times superior to multispectral ones and produce images with good contrast that gives a perfect grade of detail and a good definition of geometric properties.

On the other hand, multispectral sensors are used in many other applications: for instance they are good instruments to draw geological maps, since the number of surveys in situ and the costs are cut down.

As regards the radar sensor, they can works using many wavelenght of the signal; for instance, TerraSAR-X and Cosmo-SkyMED operate in X-band, Envisat in C-band, ALOS in L-band. The wavelenght influences the resolution of the sensor, the characteristics of interaction with the ground surface and its capability to penetrate in vegetated areas.

2.3.2 Radiometric resolution

The radiometric resolution is represented by minimum energy differences that a sensor is able to discriminate: better radiometric resolution of a sensor, more sensitive it is in detecting small energy differences.

The radiometric resolution is expressed by the number of bits used to quantize a pixel: for each bit it is recorded an exponent of power of two ($1bit = 2^1 = 2$). The maximum level of luminosity available depends on a number of bits used: for an 8 bit sensor, the digital values available are $2^8 = 256$, that means from 0 to 255 (where 0 represents the black and 255 the white).

2.3.3 Spatial resolution

The spatial resolution is the minimum ground area observed by the instrument. It is measured as the size of a pixel on the ground (also called GSD - Ground Sample Distance).

In order to make an object observable, its dimension has to be the same or bigger than the spatial resolution. The spatial resolution of the satellite imagery is classified in the Table 2.2.

Spatial resolution [m]	Class
<1	very high
1-5	high
5-20	mean
20-50	low
>50	very low

Table 2.2: Spatial resolution classes

2.4 Optical sensors actually available

In addition to optical sensor with low and medium resolution, well suited to do environmental monitoring and studies on large scale, at the present also a number of optical high resolution satellites are available. In this section the most important and most recent very high resolution sensors are listed:

- IKONOS, by GeoEye Company, launched on September 24, 1999, is the world's first commercial satellite able to collect black-and-white (panchromatic) images with 0.82 m resolution (resampled at 1 m) and 4-bands multispectral imagery with 4 m resampled resolution
- QuickBird, by Digital Globe Company, launched on October 18, 2001, is able to acquire panchromatic and 4-bands multispectral imagery, with 0.61 m and 2.44 m of resolution respectively
- WorldView-1, by Digital Globe Company, launched on September 18, 2007, is able to acquire only panchromatic imagery, with a resolution of 0.50 m
- GeoEye-1, by GeoEye Company, launched on September 6, 2008, at the moment is the world's highest resolution commercial earth-imaging satellite. It offers the best spatial resolution, by simultaneously acquiring panchromatic at 0.41 m and 4-bands multispectral imagery at 1.65 m

- WorldView-2, by Digital Globe Company, launched on October 8, 2009, is able to acquire panchromatic imagery with a resolution of 0.46 m and 8-bands multispectral imagery at 1.84 m resolution

2.5 Radar sensors actually available

Also for the radar sensor we have a large choice; in this case the sensors have a great variety of operational mode, as regard the swath extension, the polarization, the bands in which they are operating or the value of the incidence angle. These are only a few part of the sensors actually available:

- ERS-1 and ERS-2, European Remote Sensing Satellites (ERS) by ESA, are designed to study many processes of the Earth's oceans and land with a suite of instruments, one of which is a SAR. ERS-1 was launched in 1991 and ERS-2 in 1995. We could consider ERS system at the end of its life, but at the present it is still providing imagery with an across track resolution of 26 m and an azimuth resolution between 6 and 30 m

- ENVISAT, by ESA, launched in 2002, is an advanced polar-orbiting Earth observation satellite which provides measurements of the atmosphere, ocean, land, and ice, equipped with several types of sensor among which a radar sensor (Advanced Synthetic Aperture Radar - ASAR), operating at C-band. The improvements allow radar beam elevation steerage and the selection of different swaths, 100 or 400 km wide, with a spatial resolution up to 30 meter

- RADARSAT-2 is Canada's next-generation commercial SAR satellite, the follow-on to RADARSAT-1. The new satellite was launched in December, 2007. It has 0.5 m of pixel spacing in SpotLight mode, flexibility in selection of polarization, left and right-looking imaging options, it is operating in C-band

- ALOS, by Jaxa, launched in 2006. It is a Japanese system that carries a payload of three instruments, one of this is the Phased Array type L-band Synthetic Aperture Radar (PALSAR). It has great flexibility and a large number of operational mode as regard the polarization and the swath extension, in "Fine" mode it can reach about 10 meter resolution

- TerraSAR-X, by DLR, was successfully launched on June 15, 2007. With its active antenna, the spacecraft acquires high-quality X-band radar images with a resolution of up to 1 meter (SpotLight mode). TanDEM-X (TerraSAR-X Add-On for Digital Elevation Measurement) has been launched

on June 21, 2010; together they form a unique satellite formation, they are in a formation flight at distances of only a few hundred meters, able to record data synchronously in the so-called StripMap Mode (3 m ground resolution) and thus to acquire the data basis for a global Digital Elevation Model (DEM) of an unprecedented quality, accuracy, and coverage

- Cosmo-SkyMED, by ASI, has the capability to serve at the same time both civil and military users through a integrated approach (Dual Use System). The system is formed by four satellites and it has a large flexibility, as regard the swath extension and the ground resolution. The main peculiarity of Cosmo-SkyMED is the capability to acquire images with very high resolution for a SAR instrument, up to 1 meter (SpotLight mode)

Chapter 3

SAR: principles of working and applications

The term radar is an acronym for RAdio Detection And Ranging. Radar operates in radio and microwave bands of the electromagnetic spectrum ranging from a meter down to a few millimeters in wavelength. Advantages of radar include the capability to penetrate clouds, haze, rain and others atmospheric particles and to operate during night and day. Some of the most important satellites for Earth Observation are equipped with this sensor. A particular technique that uses radar is the Synthetic Aperture Radar - SAR.

3.1 The principle of Synthetic Aperture Radar

This kind of radar data processing was developed in order to improve the resolution of a traditional radar system, and it is based on the principle of Doppler frequency shift. It is an active sensor, providing its own illumination in form of microwaves, it is able to emit the signal, receive and record the signal echoes reflected by the target.

The radar signal is obtained through the conversion of an electrical current on the antenna surface induced by an electromagnetic field around this antenna and vice-versa. Thus, the received signal contains information about the scene such as dielectric properties. Firstly, we can describe the received power P_r through the radar equation:

$$P_r = \frac{P_t G^2 \lambda^2}{(4\pi)^3 R^4} \sigma \tag{3.1}$$

where P_t is the transmitted power, G is the gain of the transmitted and received antenna, λ is the wavelength of the transmitted wave, R is the slant range, that represents the distance between the radar and the scene and σ is the radar cross section.

The received power depends on many parameters such as the frequency and polarization state of the emitted wave, the dielectric nature and the shape of the object and others. For example, buildings forming a corner with the ground or other buildings, correspond to high reflected energy. Conversely, roughness surfaces diffuse the incident energy and correspond to low reflected energy [7].

The radar is on board of the satellites, having a side-looking configuration described in Figure 3.1.

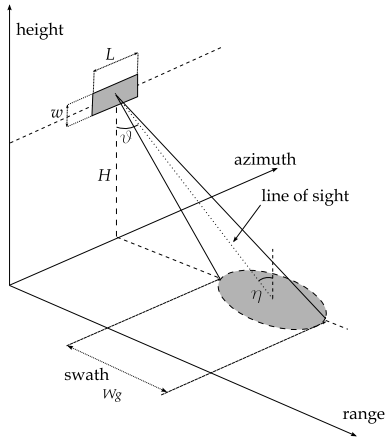

Figure 3.1: Side-looking configuration

The satellite travels forward in the flight direction or along-track (called azimuth direction) with the nadir directly beneath the platform which is at the height H. The range axis refers to the across-track dimension perpendicular to the flight direction.

The microwave beam is transmitted obliquely (with the elevation angle or side-look angle ϑ) to the direction of flight illuminating a swath. The side-looking geometry is necessary to avoid the Doppler ambiguity.

The energy emitted by the sensor impacts the target as a footprint, defined through the line of sight of the main beam of the antenna and the aperture angles (along the range and azimuth axis) of this antenna; the echo backscattered from

each ground cell within the footprint is received and recorded as a pixel in the image plane according to its position related to the azimuth and to the slant range.

The dimension of the radar antenna determines the angular field of the signal beam in azimuth direction (ω_{h}) and in cross-track direction (ω_{v}) (see Figure 3.2); more exactly this angular values are dependent from the length (L) and from the width (w) of antenna respectively, as shown in the Equations 3.2.

$$\begin{aligned} \omega_h &= \frac{\lambda}{L} \\ \omega_v &= \frac{\lambda}{w} \end{aligned} \tag{3.2}$$

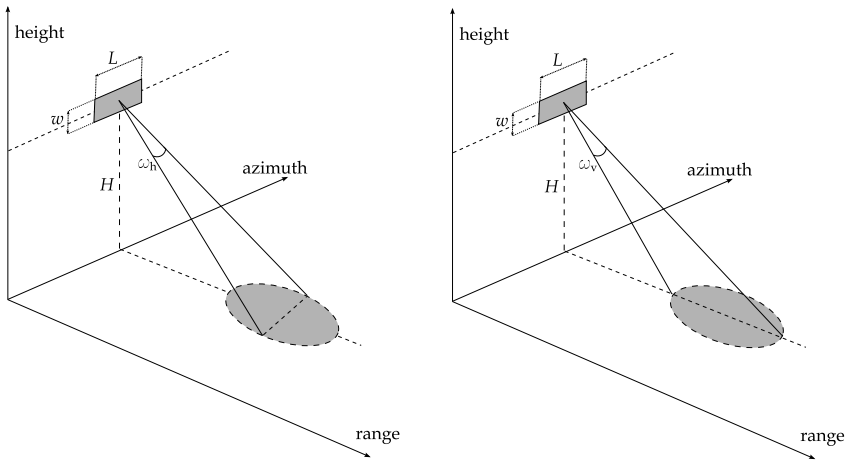

Figure 3.2: Angular field of signal in azimuth direction ω_{h} (left) and in cross-track direction ω_{v} (right)

The swath extension can be approximately expressed by the following relation:

$$W_G \approx \frac{\lambda R_m}{w \cos \eta} \tag{3.3}$$

where λ is the wavelength of the microwave used, R_m is the slant range from the center of the antenna to the center of the footprint and η is the incident angle of radar beam pulse.

The resolution of a SAR image is defined by the resolution in azimuth (Δx) and in slant range direction (ΔR), or the ground resolution in cross-track direc-

tion (Δy).

The azimuth resolution, can be expressed by the Equation 3.4, according to the electromagnetic wave theory:

$$\Delta x = \frac{R\lambda}{L} \tag{3.4}$$

where R is the slant range, λ is the wavelength of the signal and L is the length of the antenna.

The slant range and the ground range resolution can be expressed by the Equations 3.5 and 3.6:

$$\Delta R = \frac{c\tau_p}{2} \tag{3.5}$$

$$\Delta y = \frac{\Delta R}{\sin\vartheta} = \frac{c\tau_p}{2\sin\vartheta} \tag{3.6}$$

where c is the speed of light, τ_p is the pulse duration, and ϑ is the side-look angle.

The Equations 3.5 show that the slant range and the ground range resolutions are just dependent by the property of the signal, whereas the azimuth resolution is dependent by the position and size of antenna.

In order to obtain a good resolution in azimuth, the antenna should be very long; for example, a radar working in C-band ($\lambda = 5.66$ cm), with a slant range of about 700 Km (that is a plausible value for a satellite), to have 10 meters azimuth resolution, the required length of antenna should be longer than 3 Km [8].

The length of the antenna determines the real aperture, that is the space in which all echoes came back to the receiver at the same time.

The SAR system is based on the synthetic aperture principle, that simulates a longer antenna; the received signal is processed by using the fact that the radar views the scene from slightly different angles. These different views (at each emitted pulse) are obtained because the radar moves along its synthetic aperture.

The Figure 3.3 shows the acquisition process of a SAR image along its synthetic aperture. The variation of the slant range R along the image acquisition causes the frequency shift of the echo backscattered from target, varying from an increase to a decrease.

So, considering the response of one point on the ground, the reflected signal from this point can be seen as a frequency modulated signal (Doppler frequency). Also, a filtering operation, called focusing, is applied along the azimuth axis under certain assumptions (width of Doppler spectrum and duration of the seen point), consequently the azimuth resolution Δx is improved as follows:

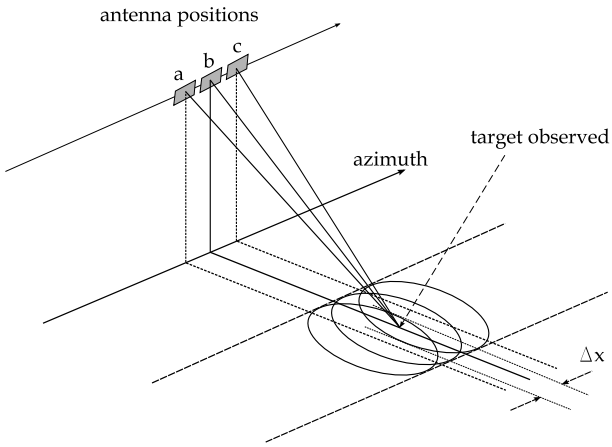

Figure 3.3: Imaging system of SAR

$$\Delta x = \frac{L}{2} \tag{3.7}$$

In this way the azimuth resolution is independent from the satellite position and it is related only to the size of antenna.

More generally, the direction of the radar pulse may be manipulated, obtaining a forward or a backward look of the radar beam. The beam is transmitted along a conical surface as shown in Figure 3.4. The axis of the cone is along the longitudinal axis of the antenna, and the squint angle τ steers the beam away from the zero-Doppler direction, that is perpendicular to the flight path.

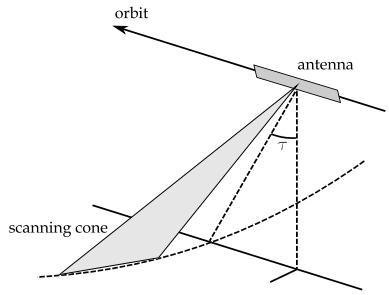

Figure 3.4: Definition of squint angle τ

The center frequency of the passage of a point scatterer through the antenna beam is called the Doppler centroid frequency, f_{CD}, whereas zero-Doppler, $f_D = 0$, denotes the direction in which the Doppler frequency is equal to zero, perpendicular to the flight direction.

The focused data of a satellite SAR image are "deskewed", that means to process the image such as the data are always observed effectively in zero-Doppler geometry.

The time of the beginning of the recorded signal is called t_{start} and the end is referred t_{end}. Also, we can define the physical limit of the radar image which is processed in the slant plane (see Figure 3.5):

- the near range $R_{near} = (c \cdot t_{start})/2$
- the far range $R_{far} = (c \cdot t_{end})/2$

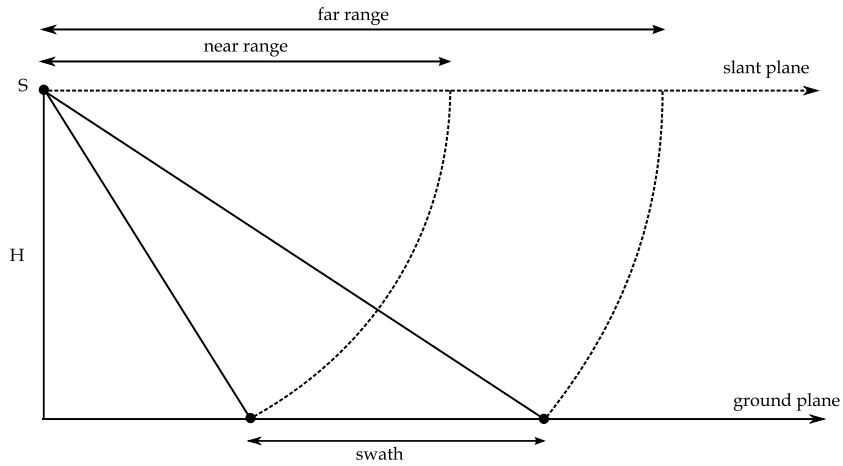

Figure 3.5: Slant range plane and ground plane projection

Taking account for the post-processing aimed at the data focusing along the synthetic aperture, the SAR image generation is possible; in this way each pixel contains the information related to its position along the azimuth, to its slant range, to the amplitude of the signal backscattered and the phase information.

The field recorded at generic pixel x, denoted $E(x)$ can be written as:

$$E(x) = \sum_{s} a(s)\exp(i\psi(s))h(s,x) \tag{3.8}$$

where the summation ranges over the scatterers, $a(s)$ and $\psi(s)$ are respectively the amplitude and phase of the signal received from scatterer s, and h is the instrument function. The value of h is near 1 when s is in or near the resolving cell corresponding to pixel x, and near zero otherwise.

The detected field E is an array of complex numbers, that represents the image. The square of the modulus of the field at x is called the detected intensity; the square-root of the intensity is called the envelope or the amplitude. This is not the same as the amplitude of the received signal because the received field is perturbed by the instrument function. The amplitude of the received signal, $a(s)$, is called the reflectivity, and its square is called the surface cross-section. Unfortunately, this is contaminated with speckle noise [9].

As regards the swath extension and the operational modes, the SAR system can image an area over the ground in stripmap mode or in spotlight mode.

In the well-known stripmap mode, the radar antenna is pointed along a fixed direction with respect to the platform flight path and the antenna footprint covers a strip on the imaged surface as the platform moves, see Figure 3.6. Accordingly, the extension of the illuminated area is theoretically unlimited in the azimuth direction, but the azimuth resolution cannot be better than a half of the real antenna azimuth length.

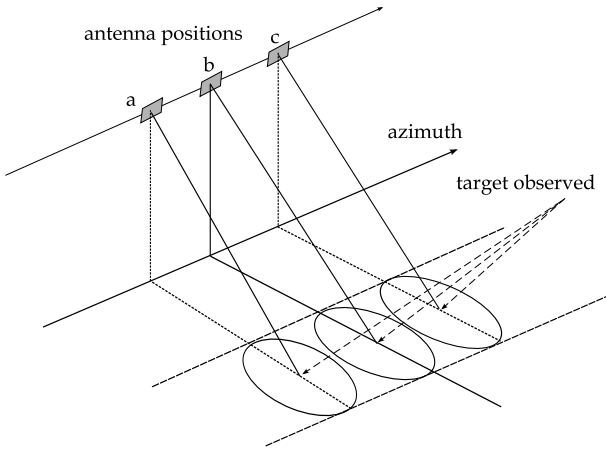

Figure 3.6: Stripmap acquisition mode

The spotlight configuration is used by the last generation satellite with high resolution, in fact in this acquisition mode the resolution in the azimuth direction is improved by increasing the synthetic aperture extension. The radar antenna beam is steered during the overall acquisition time, see Figure 3.7, thus pointing always at the same area over the ground [10].

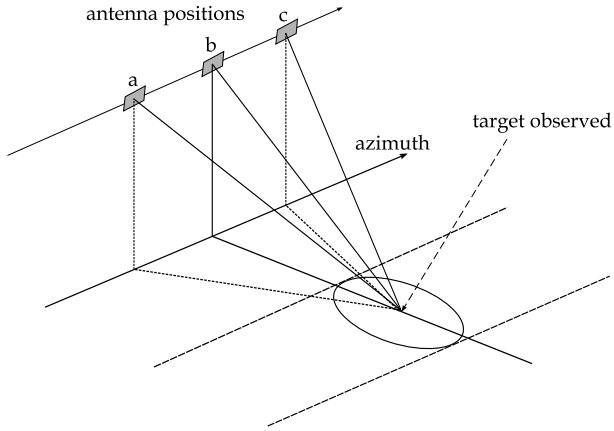

Figure 3.7: SpotLight acquisition mode

This configuration allows to obtain the best azimuth resolution to the detriment of the extension of the ground coverage.

3.2 Distortion of a radar image

The projection of a terrain slope according to SAR geometry induces well-known distortion, that in this section will be described.

In Figure 3.8 the distortion of the distance $\overline{AB}$ in ground and slant range projection is represented; the angle ACB, as defined with the auxiliary point C, is nearly equal to 90 degrees, therefore the relation between ground and slant range distance reads:

$$d_s \cong d_g \sin \vartheta_B \tag{3.9}$$

The smaller is the side-look angle, ϑ_B, to point B, the smaller is the distance in slant range projection, d_s, for a given ground distance d_g.

Now, the relief displacement on a SAR images is considered and described. Let us now consider a point A, that is situated on top of a vertical structure of height h.

From Figure 3.9 we can deduce that under the hypothesis of small height h in respect to the flying height H, the real relief displacement $A'B$ could be conveniently replaced by the displacement $A''B$, obtained through orthogonal projection. So, for a small height h, we can assume:

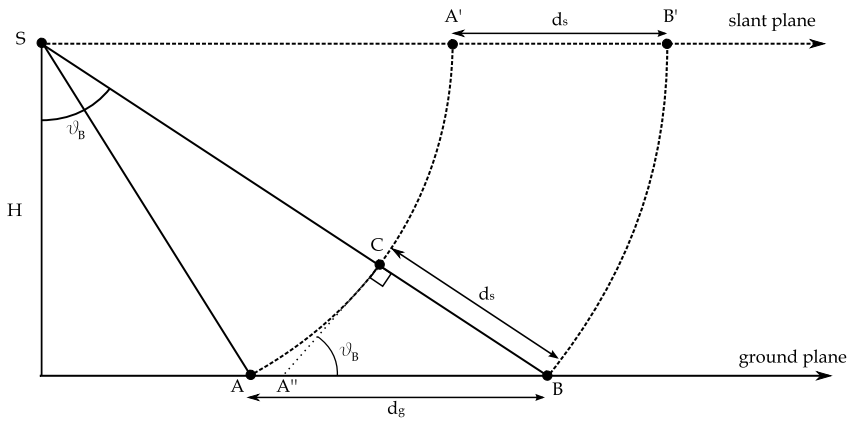

Figure 3.8: Distance $\overline{AB}$ in ground projection d_g and in slant range projection d_s

$$A'B \cong A''B \tag{3.10}$$

Under this assumption, it is possible to define simply the relief displacement in a SAR image.

In both ground and slant range projection, the relief displacement, p_g and p_s, is introduced. From Figure 3.10, using simple geometric relations, the form of the relief displacement in ground range projection reads:

$$p_g \cong h \cot \vartheta \tag{3.11}$$

The relief displacement in slant range projection reads:

$$p_s \cong h \cos \vartheta \tag{3.12}$$

The same height h produces a slightly smaller relief displacement in a slant range projection than it produces in a ground range presentation; this is the result of the overall compression of the image in a slant range projection, usual in a SAR image.

It is also obvious that the displacement increases with larger height h and with smaller side-look angles ϑ.

Another important characteristic is the direction of the displacement, that is directed toward the point of observation, whereas in classical aerial or satellite

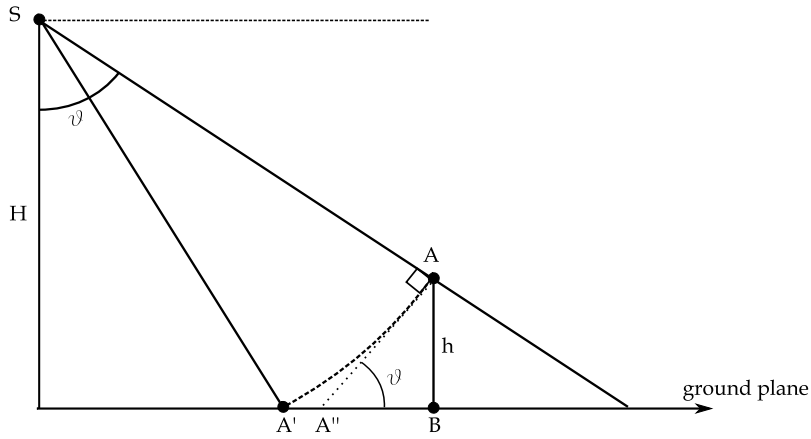

Figure 3.9: Simplifying assumption for relief displacement

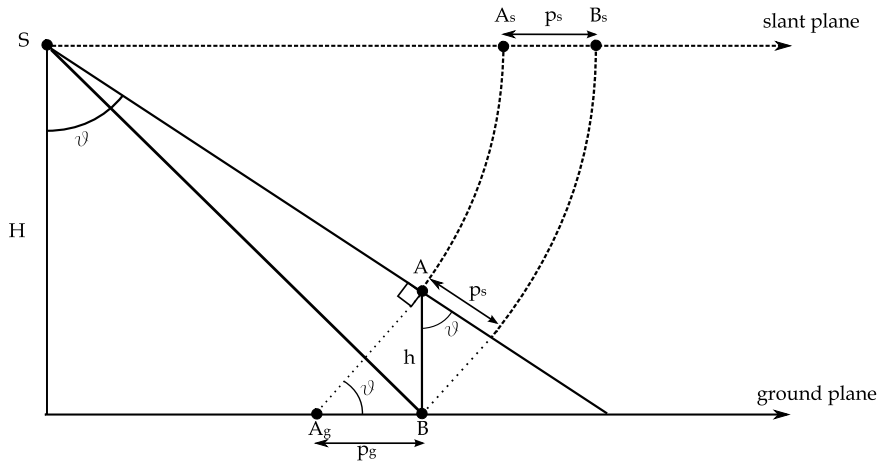

Figure 3.10: Relief displacement on a SAR image

photogrammetry it is directed away from the nadir point. This deformation is typical in SAR geometry and causes the effects called foreshortening, layover and shadows. All these effects are quite important in order to understand at best a radar image, especially in mountainous areas.

3.2.1 Foreshortening effect

The foreshortening occurs when a slope, having an aspect directed toward the satellite, is almost perpendicular the the line of sight; in this case the bottom and the top of the slope appear on the slant range projection closer than they are really (see Figure 3.11, case c). This effect is maximum when the radar beam is perpendicular to the mountain slope (see Figure 3.11, case b), where the slope might appear as a line in the image.

3.2.2 Layover effect

The layover occurs when a slope angle is greater than the side-look angle; in this case the signal reflected by the top of the slope is recorded before the signal reflected by the bottom (see Figure 3.11, case a).

3.2.3 Shadowing effect

The shadowing effect occurs when the radar beam is not able to illuminate the radar scene. This effect, that is shown in Figure 3.11, is considered as an optical shadow and induces a black area on the radar image because no reflected wave comes from this kind of region.

3.3 Principles of interferometry

The interferometry (commonly called InSAR) is by now a well known technique based on SAR data processing, widely used for environmental monitoring in remote sensing. It is the first technique we consider here for extracting 3D information from radar imagery. As mentioned it is the most used technique for DSM generation from spaceborne acquired imagery until now. It is based on the study of the phase information of SAR imagery.

Two images, acquired from slightly different points of view, can be used to form an interferogram and to derive a topographic map of the Earth's surface.

The InSAR technique derives the height information by using an interferogram in which the phase differences between two radar images are recorded. The geometric configuration suited for interferometry is described in Figure 3.12.

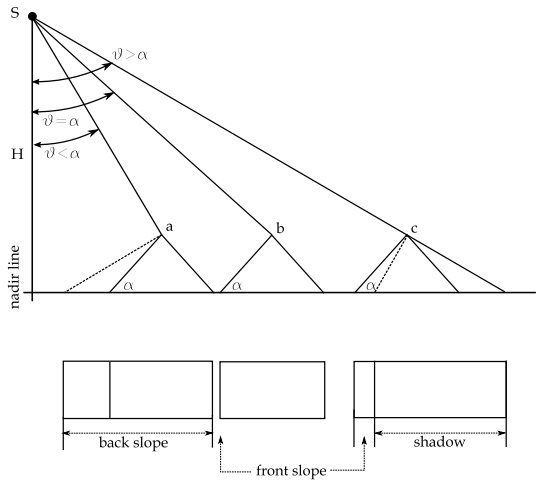

Figure 3.11: Image of slopes: layover, foreshortening and shadow effects in ground range projection

The distance between the two point of view, that is called baseline B, has to be sufficiently short.

The two images could be acquired by two different satellites or by the same satellite in different orbital passes; special "tandem" missions are operating in order to obtain the first configuration, acquiring the images with the minimum time interval to preserve the coherence of the images.

Let $\hat{S}_1(x,r)$ be the complex image acquired from the point A_1 with its phase component $\Phi_1(x,r)$ and $\hat{S}_2(x,r)$ the image acquired from the point A_2 with the phase component $\Phi_2(x,r)$.

The observed phase values ψ_1 and ψ_2 in the two images for resolution cell P are:

$$\psi_1 = -\frac{2\pi 2R_1}{\lambda} \tag{3.13}$$

$$\psi_2 = -\frac{2\pi 2R_1}{\lambda} \tag{3.14}$$

where R_1 and R_2 are the geometric distances in the two images.

The equations 3.13 and 3.14 are achieved by the conventional difference between the phase of signal emitted and the corresponding received $\psi = \varphi_{em} - \varphi_{rec}$, expressed as follows:

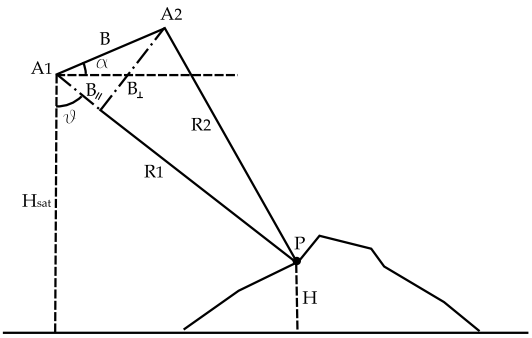

Figure 3.12: Geometry of acquisition for interferometry

$$\begin{aligned} y_{em} &= A\sin(\omega t + \varphi) \\ y_{rec} &= A\sin(\omega(t+\Delta t) + \varphi) \end{aligned} \tag{3.15}$$

$$\Delta t = \frac{2R}{c} = \frac{2R}{f\lambda} \tag{3.16}$$

$$\psi = \Delta\varphi = \omega\Delta t = \frac{2\pi}{T}\frac{2R}{f\lambda} = \frac{2\pi 2R}{\lambda} \tag{3.17}$$

where y_{em} and y_{rec} are the signal emitted and received respectively.
The interferometric phase and its derivative can be written as:

$$\phi = \psi_1 - \psi_2 = -\frac{4\pi(R_1 - R_2)}{\lambda} = -\frac{4\pi\Delta R}{\lambda} \tag{3.18}$$

$$\partial\phi = -\frac{4\pi}{\lambda}\partial\Delta R \tag{3.19}$$

Geometrically, when $B << R_1$, the difference between two slant ranges can be approximated by the baseline component in the slant range direction, $B_{||}$:

$$\Delta R \approx B_{||} = B\sin(\vartheta - \alpha) \tag{3.20}$$

where ϑ is the side-looking angle and α is the baseline orientation (see Figure 3.12).

The relation between changes in ΔR and ϑ is easily found to be:

$$\partial\Delta R = B\cos(\vartheta^0 - \alpha)\partial\vartheta \tag{3.21}$$

where the initial value of ϑ^0 is obtained for the reference surface. The relation

between an interferometric phase change and the change of side-looking angle can be found through equations 3.19 and 3.21:

$$\partial\phi = -\frac{4\pi}{\lambda} B \cos(\vartheta^0 - \alpha)\partial\vartheta \tag{3.22}$$

The interferometric phase change can be defined as the difference between the measured phase ϕ and the expected phase for the reference surface θ derived from the orbit geometry:

$$\partial\phi = \phi - \theta \tag{3.23}$$

The height of the satellite above the reference surface is known, and it is expressed by:

$$H_{sat} = R_1 \cos\vartheta \tag{3.24}$$

and the derivative for a resolution cell P with range R_1 gives the relationship between a change in look angle ϑ due to a height difference ∂H_{sat}:

$$\partial H_{sat} = -\partial H = -R_1 \sin\vartheta^0 \partial\vartheta \tag{3.25}$$

Using 3.22 and 3.25 we derive the relationship between $-\partial H$ (the height above the reference surface) and the phase difference $\partial\phi$

$$-\partial H = -\frac{\lambda R_1 \sin\vartheta^0}{4\pi B_\perp^0}\partial\phi \tag{3.26}$$

which is the fundamental equation to retrieve the height H of the cell P with respect to the chosen reference surface, with

$$B_\perp^0 = B\cos(\vartheta^0 - \alpha) \tag{3.27}$$

The initial value of ϑ^0 is found for an arbitrary reference surface (e.g., sphere or ellipsoid).

The main steps for the height determination are:

- images co-registration, the images need to be in the same coordinate system
- interferogram generation
- phase unwrapping

As regards the third step, it has to be underlined that the phase difference corresponds to a number of whole waves (ϕ_u) plus a residual (ϕ_o):

$$\phi = \phi_u + \phi_o = 2\pi k + \phi_o \tag{3.28}$$

where k is a integer, and it is undetermined. This is a cycle ambiguity problem, that can be solved by the phase unwrapping, using information about the phase differences in neighboring pixels [8].

A particular technique based on interferometric principle is the Differential Interferometry (DInSAR), which aims at the measurement of ground deformation using repeat-pass. Since line of sight displacement enter directly into the interferogram, independent of the baseline, it can be measured as a fraction of the wavelength. Unfortunately, non-zero baseline causes some sensitivity with regard to topography in the interferogram. So, an elevation model has to be used, in order to subtract it from the interferogram.

SAR interferometry only works when the coherence is preserved and maintained between the two SAR images, since the received reflections have to be correlated. Loss of coherence, known as decorrelation, can be due to a large number of causes; some sources of decorrelation can be reduced using filtering procedures, others sources are more significant and non-reversible. Temporal decorrelation, for example, is an important limitation for the application of repeat-pass interferometry, that consists of the variation of the physical distribution of the elementary scatterers; weathering, vegetation, or anthropogenic activities are common causes of temporal decorrelation [11].

3.4 Principles of radargrammetry

Radargrammetry is a second technique for extracting 3D information from radar imagery.

In analogy to photogrammetry, radargrammetry forms a stereo model for 3D measurement.

Just to summarize the fundamentals, in photogrammetry, "stereoscopy is the science and art that deals with the use of images to produce a three-dimensional visual model with characteristics analogous to that of actual features viewed using true binocular vision"[12].

In the stereoscopic space perception, two major cues are used: the convergence and the binocular disparity. Convergence is the ability to focus the optical axes of the two eyes on to a single object. The sensing of the amount of muscular tension in the eyes resulting from different convergence angles provides a cue to the absolute distance to the viewed point. The binocular disparity (or parallax) is the difference between the images of an object projected on to each retina. The degree of disparity between the two projected images depends on the convergence angle. The binocular disparity is considered the most important perception cue over medium distance, and is the only one used in stereo photo or radargrammetry for quantitative elevation extraction [13].

The differences between images can be measured to establish a disparity map, that is used in radargrammetry to compute the terrain elevation from the measured parallaxes between the two images.

A simplified model is shown in Figure 3.13, where the area is flat, the flight lines are parallel and the height flight is constant; the Equation 3.29 is the relation for the height computation in case of slant-range projection, where h denotes the height of the scattered point, $p_{1,2}$ the absolute parallax and $\vartheta_{1,2}$ the incidence angles, the denominator sign "$\pm$" depends on the flight configuration, "+" for opposite-side and "$-$" for same-side stereo pair [14].

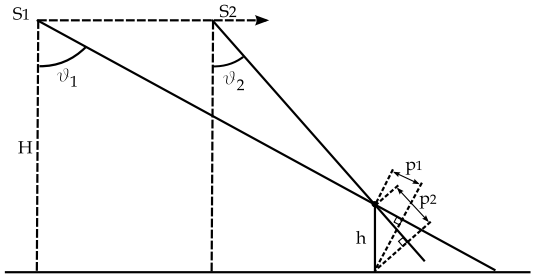

Figure 3.13: Terrain height computation using the parallaxes

$$h = (p_1 - p_2)/(\cos\vartheta_2 \pm \cos\vartheta_1) \tag{3.29}$$

In the 1960s, stereoscopic methods were first applied to radar images to derive ground elevation leading to the development of radargrammetry [15]. It was shown that some specific SAR stereo configurations would produce the same elevation parallaxes as those produced by aerial photos.

To obtain good stereo geometry, the optimum configuration for the radargrammetric application is when the target is observed in opposite-side view (see Figure 3.14); the intersection angle should be large in order to increase the parallax, that is to better determine the terrain elevation.

Conversely, a small intersection angle implies a good stereo viewing, having a stereo-pair as nearly identical as possible.

Opposite-side view, and large intersection angle cause large geometric and radiometric disparities hindering the image matching, that is the identification of the corresponding imaged points and the second fundamental step for 3D object reconstruction and therefore for DSMs generation after the imagery orientation, that is the stereo imagery georeferencing and attitude determination, as for the standard photogrammetric processing applied to imagery acquired from airborne and spaceborne sensors. A good compromise is to use a same-side configuration

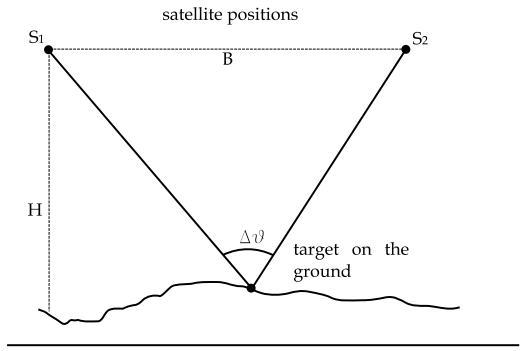

Figure 3.14: Stereo opposite-side for radargrammetry

stereo pair (Figure 3.15) with a base to height ratio ranging from 0.25 to 2.0 [7] in order to increase the efficiency in the correlation image process.

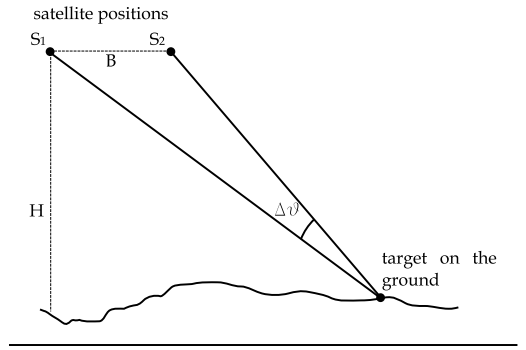

Figure 3.15: Stereo same-side configuration for radargrammetry

Only the amplitude information of a SAR images is used for radargrammetric measurement, whereas the interferometry uses the phase information.

An amplitude SAR image is similar to an optical image, obviously having different effects of distortion (see Section 3.2). The gray tones of the image depend on several characteristics of the imaged surface, since the radar scene reflects a certain amount of radiation according to its geometrical and physical characteristics.

The electrical properties of the soil and the roughness of the area are crucial; moreover, as we have seen before, the geometric shape of an area or an object on the ground mainly determines the radiometry of a pixel and the brightness

of a feature could be a combination with other objects. Another important parameter is the wavelength of the incident radiation wave and the electromagnetic interaction falls with either surface interaction or volume interaction [7].

Also, we can separate the interactions into two main topics:

- specular reflection: smooth surfaces that reflect all the incident waves; when the surface is tilted toward the radar the corresponding radar image appears very bright, conversely, if the surface is not turned toward the radar (e.g. calm water or paved roads), the surface appears dark on the radar image

- diffuse reflector: rough surface that scatters the incident wave in many directions

Also the side-look angle influences the signal reflection.

A typical phenomenon that occurs specially in urban area is the double bounce reflection, caused by the so-called corner reflector. This kind of object are characterized by two (or more) surfaces (generally smooth) forming a right angle, and are very common in urban areas. They appear as very clear targets on the radar image, indicated by a bright line, as shown in Figure 3.16, that represents an example of TerraSAR-X image in the urban area of Hannover [16].

Figure 3.16: Double bounce effect in Hannover urban area, TerraSAR-X image

As regards the radiometric features of a SAR image, an important effect is the speckle noise, that looks like a "salt and pepper" texture. This texture is due to the chaotic response of multiple small targets on the ground, whose global response is seen as a constructive or destructive random process.

Numerous researches were dedicated to the speckle noise and to its elimination or reduction by image filtering (as example [9],[17],[18],[19]), since this effect is seen as a multiplicative noise and degrades the quality of a radar image.

As regards the radargrammteric model, figure 3.17 shows a general same-side configuration, in which the scene is observed from two different point of view with two different look angles.

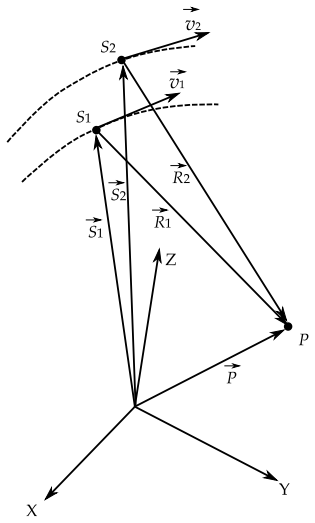

Figure 3.17: Basic stereo geometry for radargrammetry

Let S_1 and S_2 be the sensor positions, the object position P can be determined by the intersection of two radar rays with different look angles, leading a coplanarity condition expressed by:

$$\vec{S_1} + \vec{R_1} - \vec{S_2} - \vec{R_2} = 0 \tag{3.30}$$

where $\vec{S_1}$ and $\vec{S_2}$ denote the position vectors of sensors 1 and 2, while $\vec{R_1}$ and $\vec{R_2}$ denote the sensor-object vectors of two radar rays. The above conditions can be interpreted as the intersection of range spheres and Doppler cones, and thus we have two range equations and two Doppler equations given as follows:

Range equation:

$$\begin{aligned} \left|\vec{P} - \vec{S_1}\right| &= \left|\vec{R_1}\right| = R_1 \\ \left|\vec{P} - \vec{S_2}\right| &= \left|\vec{R_2}\right| = R_2 \end{aligned} \tag{3.31}$$

Doppler equation:

$$\begin{aligned} \vec{v_1}(\vec{P} - \vec{S_1}) &= 0 \\ \vec{v_2}(\vec{P} - \vec{S_2}) &= 0 \end{aligned} \tag{3.32}$$

where $\vec{v_1}$ and $\vec{v_2}$ denote the 3D velocity vectors of sensors 1 and 2. The equations 3.31 and 3.32 represent the general case of zero-Doppler projection [8].

These four equations represent the base for the stereo model of radargrammetry; further details will be discussed in Chapter 4.

3.4.1 State of the art of radargrammetry

As mentioned, the radargrammetric approach was first used in the 1960s [15]; then, it was less and less used, due to the quite low resolution in amplitude of radar image, if compared to their high resolution in phase.

In the past radagrammetric applications was related both to aerial and to satellite sensors; as regards satellite sensors, in the last twenty years, some researchers have investigated the DSMs generation from SAR data acquired by the various sensors presently available. Some of results published in scientific literature are presented in this section.

Toutin has published numerous works in the field of remote sensing and DSMs generation from optical and SAR data (to this aim see [1]). His investigations concerned at first radargrammetric applications with low resolution satellite, as ERS-1 and RADARSAT-1.

As regards ERS-1, its SAR instrument has a spatial resolution of 30 m; the DSM accuracy achievable from it in Toutin's works is about 24 m in [20] and in [21], and about 20 m in [2].

Moreover Toutin was involved in investigations related to the Canadian satellite RADARSAT-1, that have a spatial resolution up to 10 m in Fine mode; he studied about the possibilities to use same side or opposite side stereo pair, and about the relation between the DSM accuracy and the slope and aspect of the terrain relief [22].

By comparing the results for low and moderate relief, Toutin found that the relief is an important parameter that has an impact on the DEM accuracy. However, large radiometric disparities in the stereo pair depending on different factors related to SAR and surface interaction (moisture, roughness, vegetation, foreshortening, etc.) should affect the DEM accuracy; in fact, high radiometric disparities could invalidate results also in case of good geometric configuration of stereo images [23].

DSM errors for RADARSAT-1 are at level of tens of meters, however, as mentioned; results are depending from stereo configuration, radiometric disparities or soil coverage and topography; for instance, DSM accuracy is almost linearly correlated with the terrain slopes [24].

Meric, Fayard and Pottier carried on some investigations about radargrammetric applications with SIR-C/X-SAR mission. In the Austran Alps, with a pixel size of 25 m, we have a percentage error of: 45% from 0 to 70 m, 40% from 70 to 130 m, and 15% from 130 to 200 m [14].

Crosetto studied radargrammetric applications with RADARSAT-1 and the

potentialities of integration and fusion of radargrammetric and interferometric results, in order to obtain the best (accurate and complete) product [25].

Overall, the global accuracy achievable with old generation SAR sensors was around tens of meters.

Now the goal is to improve the radargrammteric DSM accuracy using the new generation sensors. To this end we recall the investigation of the research group of "Joanneum Research Institute" about TerraSAR-X satellite.

Some results was been published in [3], where, for flat areas, the mean height differences are close to zero, while the standard deviation is about 3 m, while for forested terrain, mean values are between about 12 and 20 m, as well as standard deviations around 4 m. They investigated also the possibility to use a block of three SAR images.

Again, Toutin has published results about the application of his radargrammetric model to RADARSAT-2 imagery [4]; results of preliminary geometric calibration are at level of 2 meters in height component for images in Ultrafine mode (1.56 m $\times$ 1.56 m pixel spacing).

Chapter 4

Radargrammetric model implemented in SISAR

4.1 Coordinate systems

In order to introduce the collinearity equations, the definitions of some coordinate systems are needed [26]:

Earth-Centered Earth-Fixed system - ECEF (E): the origin is in the Earth center of mass, the X_E-axis is the intersection of equatorial plane and the plane of reference meridian (epoch 1984.0), the Z_E-axis is the mean rotational axis (epoch 1984.0) and the Y_E-axis completes the right-handed coordinate system [27], [28], (Figure 4.1*b*).

Earth Centered Inertial system - ECI (I): the origin is in the Earth center of mass, the X_I-axis points to vernal equinox (epoch J2000 - 1 January 2000, hours 12 UT), the Z_I-axis points to celestial north pole (epoch J2000) and the Y_I-axis completes the right-handed coordinate system [27], [28], (Figure 4.1*a*).

Image system (I): The image coordinate system is 2D and describes the position of a point in an image: the origin is in the upper left corner, the position is pointed out by its line (J) and sample (I); the line number increases downwards and the sample number increases toward the right (Figure 4.2b).

The line number J is related to the acquisition time, measured along the

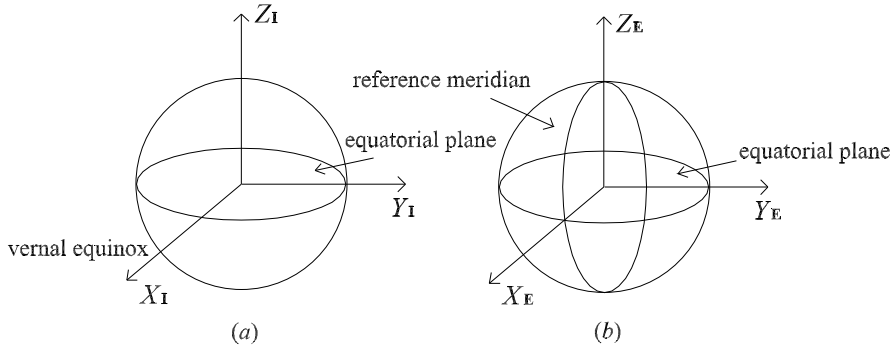

Figure 4.1: Coordinates in the Earth Centered Inertial - ECI (a) and in the Earth-Centered Earth-Fixed - ECEF (b)

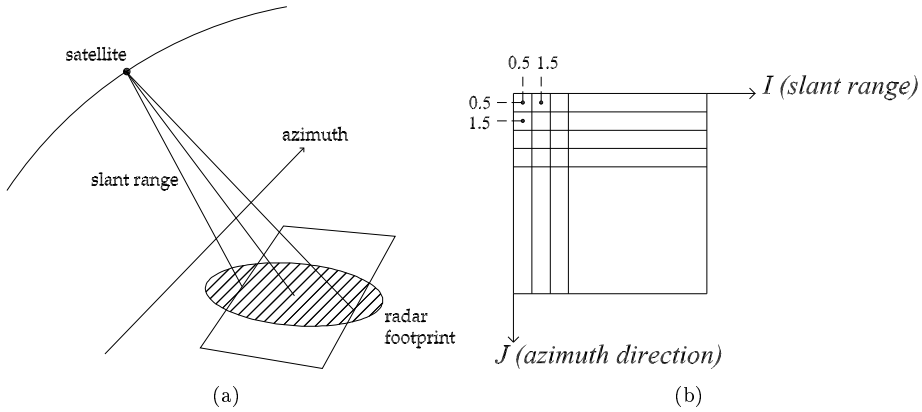

Figure 4.2: Image acqusition system (a) and azimuth and slant range direction in the image reference system (b)

flying direction of the satellite (azimuth direction); the sample number I is related to the slant range of each point, that is the distance between the satellite and the imaged point on the ground.

Correspondingly, as already underlined, the pixel dimension is characterized by two different resolutions: the azimuth resolution in flying direction (or line

spacing Δl) and the slant range resolution in the slant range direction (column spacing Δr).

Orbital system (O): the $X_O - Y_O$ plane coincides with the orbital plane, which is defined by right ascension of the ascending node (Ω) and by the orbit inclination (i). X_O-axis is along the nodal line, Y_O-axis and Z_O-axis complete the right-handed coordinate system. With the hypothesis of Keplerian orbit, Z_O-coordinate of satellite in the orbital system is zero (Figure 4.3).

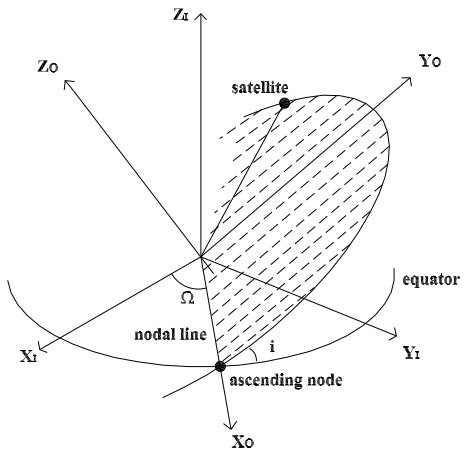

Figure 4.3: Coordinates in the Orbital system

Geodetic local system (L): the origin is a chosen point on the ellipsoid (here the WGS84 is used) the *North*-axis is tangent to the local meridian, *East*-axis is tangent to the local parallel and *Up*-axis (elevation axis) is along the ellipsoid normal (Figure 4.4).

4.2 Coordinate System Transformations

4.2.1 ECI system - ECEF system transformation

The rotation matrix for the transformation from ECI system to ECEF system ($\mathbf{R}_{EI}$) can be subdivided into four sequential steps, considering the motions of the Earth in space: precession, the secular change in the orientation of the Earth's rotation axis and of the vernal equinox (described by the matrix $\mathbf{R}_P$); nutation, the periodic and short-term variation of the equator and of the vernal equinox (described by the matrix $\mathbf{R}_N$); polar motion, the coordinates of the rotation axis

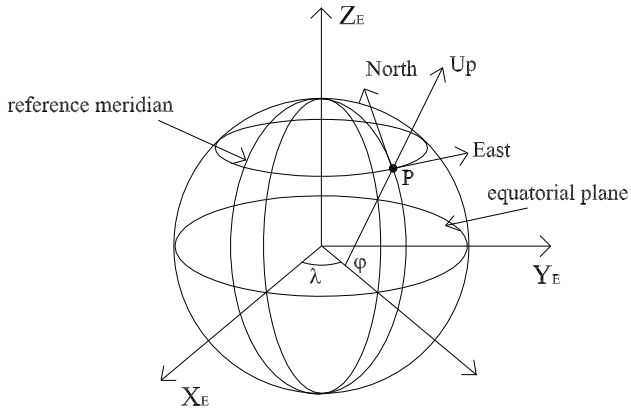

Figure 4.4: Coordinates in the Geodetic Local system

relative to the IERS Reference Pole (described by the matrix $\mathbf{R}_M$); and Earth's rotation about its axis (described by the Sideral Time through the matrix $\mathbf{R}_S$) [29].

$$\mathbf{R}_{EI} = \mathbf{R}_M \cdot \mathbf{R}_S \cdot \mathbf{R}_N \cdot \mathbf{R}_P \tag{4.1}$$

- $\mathbf{R}_P$ **(Precession matrix)**: it describes the effect of precession motion that represents the rotation from celestial equator at epoch J2000 (1st January 2000, 12hUT1) to a system defined by mean celestial equator at generic epoch t [29].

$$\mathbf{R}_P = \mathbf{R}_Z(-z)\mathbf{R}_Y(\theta)\mathbf{R}_X(\xi) \tag{4.2}$$

where the three angles z, θ and ξ are determined by Nautical Almanac Office ($\mathbf{R}_X$, $\mathbf{R}_Y$, $\mathbf{R}_Z$ are the generic rotation matrices around X, Y, Z axes). [1]

[1] Generic form of the rotation matrices around the X, Y, Z axes

$$\mathbf{R}_X(\alpha) = \begin{bmatrix} 1 & 0 & 0 \\ 0 & \cos(\alpha) & \sin(\alpha) \\ 0 & -\sin(\alpha) & \cos(\alpha) \end{bmatrix}$$

$$\mathbf{R}_Y(\beta) = \begin{bmatrix} \cos(\beta) & 0 & -\sin(\beta) \\ 0 & 1 & 0 \\ \sin(\beta) & 0 & \cos(\beta) \end{bmatrix}$$

$$\mathbf{R}_Z(\gamma) = \begin{bmatrix} \cos(\gamma) & \sin(\gamma) & 0 \\ -\sin(\gamma) & \cos(\gamma) & 0 \\ 0 & 0 & 1 \end{bmatrix}$$

- $\mathbf{R}_N$ **(Nutation matrix)**: it describes the effect of nutation motion that represents the rotation from a system defined by mean celestial equator at generic epoch t to a system defined by true celestial equator at the same epoch, in this system the Z-axis is the instantaneous rotation axis of the Earth. The main contributions to nutation come from the varying orientation of the lunar orbit with respect to the Earth's equator as expressed by the longitude of the Moon's ascending node Ω_m. It induces a period shift of the vernal equinox ($\Delta\psi \propto \sin\Omega$) and a change of the obliquity of the ecliptic ($\Delta\epsilon \propto \cos\Omega$) during the 18.6 year nodal period of the Moon [29].

$$\mathbf{R}_N = \mathbf{R}_X(-(\epsilon + \Delta\epsilon))\mathbf{R}_Z(-\Delta\psi)\mathbf{R}_X(\epsilon) \tag{4.3}$$

  where ϵ is the mean obliquity of the ecliptic.

- $\mathbf{R}_S$ **(Sideral matrix)**: it describes the effect of Earth's rotation around its instantaneous rotation axis, that is the rotation between the system defined by true celestial equator at generic epoch t and an instantaneous system where the X-axis passing through the intersection between the instantaneous Earth's equator and the instantaneous Greenwich meridian. The matrix is a function of GAST-Greenwich Apparent Sideral Time $\mathbf{R}_S = \mathbf{R}_z(GAST)$ [29].

- $\mathbf{R}_M$ **(Polar Motion matrix)**: it describes the periodic motion of Celestial Ephemeris Pole with respect to the surface of the Earth that is the motion of the Earth with respect to its instantaneous rotation axis; this is a function of instantaneous pole coordinates, available by IERS (International Earth Rotation Service) [30].

$$\mathbf{R}_M = \mathbf{R}_X(-y_P)\mathbf{R}_Y(-x_P) \tag{4.4}$$

- **Greenwich Apparent Sideral Time - GAST**: the GAST measures the hour angle of the true equinox; it is a function of GMST - Greenwich Mean Sideral Time and of the nutation in right ascension.

$$GAST = GMST + \Delta\psi\cos\epsilon \tag{4.5}$$

  GMST denotes the angle between the mean vernal equinox of date and the Greenwich meridian, it is a time function calculated adding the value of GMST at midnight (0^h) of the day of interest and the angular rotation of the Earth between 0^h and t of the day of interest (Δt) [29]:

$$GMST = GMST_0 + \omega_\epsilon \Delta t \tag{4.6}$$

$$GMST_0 = 24110.54841 + 8640184.812866 \cdot T_0 + 0.093104 \cdot T_0^2 - 6.2 \cdot 10^{-6} \cdot T_0^3 \quad (4.7)$$

where ω_ϵ is the Earth's rotation rate ($\omega_\epsilon = 7.29 \times 10^{-5} rad/sec$) and T_0 is the number of Julian centuries of Universal Time (UT1) elapsed since the epoch J2000.

$$T_0 = \frac{JD - 2451545}{36525} \quad (4.8)$$

4.2.2 ECI system - Orbital system transformation

The conversion from ECI system (I) to Orbital system (O) can be performed using the relation 4.9 based on the rotation matrix 4.10. The parameters of the matrix are the right ascension of the ascending node (Ω) and by the orbit inclination (i).

$$\begin{vmatrix} X_O \\ Y_O \\ Z_O \end{vmatrix} = \mathbf{R}_{I \to O} \cdot \begin{vmatrix} X_I \\ Y_I \\ Z_I \end{vmatrix} \quad (4.9)$$

$$\mathbf{R}_{I \to O} = \begin{bmatrix} \cos\Omega & \sin\Omega & 0 \\ -\sin\Omega\cos i & \cos i\cos\Omega & \sin i \\ \sin i\sin\Omega & -\sin i\cos\Omega & \cos i \end{bmatrix} \quad (4.10)$$

4.2.3 ECEF system - Geodetic Local system transformation

The conversion from ECEF system (E) to geodetic Local system (L) can be performed using the relation 4.11 based on the rotation matrix 4.12. The parameters of the rotation matrix are latitude (φ) and longitude (λ) of the geodetic system origin; the parameters T_X, T_Y, T_Z of 4.11 are the translation components and they are represented by the geodetic system origin coordinates in ECEF system.

$$\begin{vmatrix} X_L \\ Y_L \\ Z_L \end{vmatrix} = \begin{vmatrix} East \\ North \\ Up \end{vmatrix} = \mathbf{R}_{E \to L} \begin{vmatrix} X_E - T_X \\ Y_E - T_Y \\ Z_E - T_Z \end{vmatrix} \quad (4.11)$$

$$\mathbf{R}_{E \to L} = \begin{bmatrix} -\sin\lambda & \cos\lambda & 0 \\ -\sin\varphi\cos\lambda & -\sin\varphi\sin\lambda & \cos\varphi \\ \cos\varphi\cos\lambda & \cos\varphi\sin\lambda & \sin\varphi \end{bmatrix} \quad (4.12)$$

4.3 General projection equations

In this section the classical equation proposed by Leberl [5] are described; they can be considered the basis for the developing of the model. Hereafter further details about the model implemented in SISAR are pointed out, regarding the parameters estimated and the orbit refinement.

Considering Figure 4.5, the object system (that simply could be a geodetic local system) and the sensor system are defined and represented with unit vector e_x, e_y, e_z and $\hat{u}, \hat{v}, \hat{w}$ respectively.

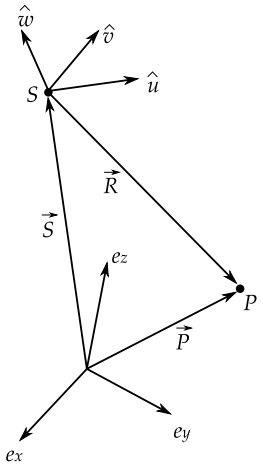

Figure 4.5: Definition of object space and sensor coordinate system

The sensor position is defined as follows:

$$\vec{S}(t) = [S_x(t), S_y(t), S_z(t)]^T \tag{4.13}$$

while antenna attitude is represented by the angles $\varphi(t), \theta(t), \psi(t)$.
The derivative of the satellite position is the satellite velocity:

$$\dot{\vec{S}}(t) = [\dot{S}_x(t), \dot{S}_y(t), \dot{S}_z(t)]^T \tag{4.14}$$

For an object point P, its position vector in the object system $\vec{P}$ is:

$$\vec{P} = P_x e_x + P_y e_y + P_z e_z \tag{4.15}$$

and in the sensor system is:

$$\vec{P^*} = u_P\hat{u} + v_P\hat{v} + w_P\hat{w} \tag{4.16}$$

The coefficients u_P, v_P, w_P, that define the point position in sensor system, can be represented by the following relations:

$$\begin{aligned} u_P &= R_s \sin\tau \\ v_P &= R_s(\sin^2\vartheta - \sin^2\tau)^{1/2} \\ w_P &= -R_s\cos\vartheta \end{aligned} \tag{4.17}$$

where R_s is the module of the vector $\vec{R}$, ϑ is the side-look angle and τ is the squint angle. The Equations 4.17 is valid in the general case in which the squint angle τ is different from zero, and the imaging of surface is in a plane that is not perpendicular to the flight direction. In a zero-Doppler projection, when $\tau = 0$, the Equations 4.17 became:

$$\begin{aligned} u_P &= 0 \\ v_P &= R_s \sin\vartheta \\ w_P &= -R_s\cos\vartheta \end{aligned} \tag{4.18}$$

Vector $\vec{P}^*$ is obtained in the sensor system, and the vector $\vec{P}$ in the object system. The rotation matrix $\mathbf{R}$ is suited to rotate the sensor system $\hat{u}, \hat{v}, \hat{w}$ in the object system e_x, e_y, e_z, and it relates vectors $\vec{P}^*$ and $\vec{P}$ as follows:

$$\vec{P} = \vec{S} + \mathbf{R}\vec{P}^* \tag{4.19}$$

where $\mathbf{R}$ is:

$$\mathbf{R} = \begin{bmatrix} u_x(t) & u_y(t) & u_z(t) \\ v_x(t) & v_y(t) & v_z(t) \\ w_x(t) & w_y(t) & w_z(t) \end{bmatrix} \tag{4.20}$$

With synthetic antenna we obtain:

$$\begin{aligned} \hat{u} &= (u_x, u_y, u_z) = \vec{S}/|\vec{S}| \\ \hat{v} &= (v_x, v_y, v_z) = (\vec{S} \times \vec{\dot{S}})/|\vec{S} \times \vec{\dot{S}}| \\ \hat{w} &= (w_x, w_y, w_z) = (\hat{u} \times \hat{v})/|\hat{u} \times \hat{v}| \end{aligned} \tag{4.21}$$

The unit vector $\hat{u}$ is directed along the synthetic antenna, as the satellite

velocity vector $\dot{S}$. The unit vector $\hat{v}$ should be normal to $\hat{u}$ and to nadir direction of antenna.

The Equations 4.17 and 4.19 relate the object and the image, since the slant range R_s and the time t derive from the image coordinates.

If $\vec{S}(t)$ and $\mathbf{R}(t)$ are known as function of the time t, then for each point we have three equations (Equation 4.19) with four unknowns $(\vartheta, P_x, P_y, P_z)$; in place of them, it could be preferable to work with two equations with three unknowns, eliminating the look angle ϑ. We form the relations:

$$|\vec{P} - \vec{S}| = R_s \tag{4.22}$$

$$\hat{u} \cdot (\vec{P} - \vec{S}) = \sin\tau \cdot |\hat{u}| \cdot |\vec{P} - \vec{S}| = \sin\tau \cdot R_s \tag{4.23}$$

We also recall the following relations:

$$\frac{u_p}{[v_p^2 + w_p^2]^{1/2}} = \tan\tau \tag{4.24}$$

$$(u_p^2 + v_p^2 + w_p^2)^{1/2} = R_s \tag{4.25}$$

The previous equations are related to a general case in which the squint angle τ is different from zero; in particular, when the image is acquired in zero-Doppler geometry, the Equation 4.23 becomes:

$$\hat{u} \cdot (\vec{P} - \vec{S}) = 0 \tag{4.26}$$

where $\hat{u}$ is the unit vector directed as the satellite velocity vector $\dot{S}$.

The Equations 4.22 and 4.23 correspond to the intersection of a range sphere, defined by the slant range R_s, with a cone, defined by the squint angle τ. In zero-Doppler case, the range sphere intersects a plane perpendicular to the flight direction (the cone degenerates to a plane). This intersection produces a "Doppler circle" (see Figure 4.6).

Finally, note that the squint angle is defined as a function of the reference Doppler frequency used for the image generation, f_D, that is expressed by:

$$f_D = \frac{2}{\lambda R_s} \hat{u}(\vec{S} - \vec{P}) \tag{4.27}$$

Consequently the squint angle results from:

$$\sin\tau = \frac{\lambda f_D}{2} \tag{4.28}$$

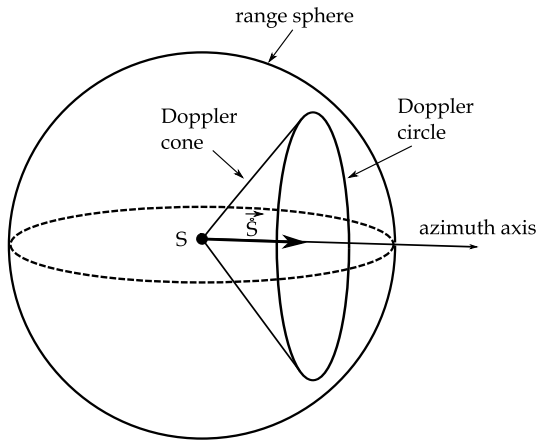

Figure 4.6: Range sphere, Doppler cone and Doppler circle

4.4 The radargrammetric model implemented in SISAR

In this section more details about the model implemented in SISAR software for SpotLight imagery are described.

The radargrammetric approach performs a 3D reconstruction based on the determination of the sensor-object stereo model, in which the object position is computed by the intersection of two radar rays with two different look angles.

More exactly, as explained in the previous section, the Equations 4.22 and 4.23 (or Equations 4.22 and 4.26 in zero-Doppler projection) define a Doppler circle. Thus, in a stereo configuration, using at least a couple of images, the object position of a generic point is determined by the intersection of two Doppler circles (see Figure 4.7); in this way we have four equations and three ground coordinates unknowns.

The SISAR model is based on the assumption of zero-Doppler projection, that usually is the common projection in which the SAR imagery are distributed, since they are subjected to a focusing process. In this sense, we could refer to Equations 4.22 and 4.26, that can be expressed in a geodetic local system, with the origin in the image center (known from ancillary data).

As described above, the Equation (4.22) is the slant range constrain, whereas the Equation 4.26 represents the general case of zero-Doppler projection, in which the target is acquired on a heading that is perpendicular to the flying direction of satellite.

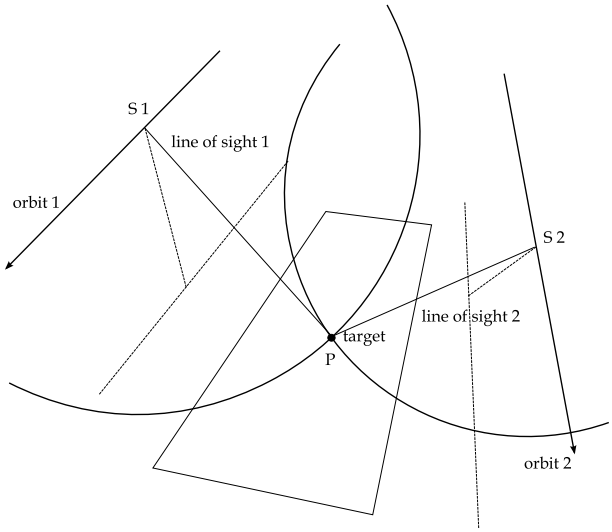

Figure 4.7: Intersection of Doppler circles in stereo configuration

The Equations 4.22 and 4.26, in explicit form, read:

$$\begin{cases} \sqrt{(X_P - X_S)^2 + (Y_P - Y_S)^2 + (Z_P - Z_S)^2} - (D_s + \Delta r \cdot I) = 0 \\ u_{S_X} \cdot (X_P - X_S) + u_{S_Y} \cdot (Y_P - Y_S) + u_{S_Z} \cdot (Z_P - Z_S) = 0 \end{cases} \tag{4.29}$$

where:

- X_P, Y_P, Z_P are the coordinates of the generic ground point P in the local coordinate system (time independent)
- X_S, Y_S, Z_S are the coordinates of the satellite in the local coordinate system (time dependent)
- u_{X_S}, u_{Y_S}, u_{Z_S} are the cartesian components of the satellite velocity in the local coordinate system (time dependent)
- D_s is the so-called "near range"
- Δr is the slant range resolution or column spacing
- I is the column position of point P on the image

4.4.1 Satellite coordinates

As regards the satellite position computation, the basic assumption is that the orbital arc related to the image acquisition in SpotLight mode is quite short (about 10 Km), so that it could be conveniently modeled with a circular arc.

Circumference parameters are estimated by least squares adjustment using few orbital state vectors available in the ancillary data; the state vectors contain the satellite coordinates, expressed in ECI or ECEF system, generally sampled at regular interval times (for example 10 seconds) before and after the image acquisition. Using this information it is possible to reconstruct the orbital segment related to the SAR image.

The circular model is set up in the orbital coordinate system, defined by the orbit inclination i and the right ascension of the ascending node Ω, that are orbital parameters computed from the state vectors. Satellite positions of the state vectors are transformed in the orbital system using the rotation matrix $\mathbf{R}_{I \to O}$, as described in Section 4.2.2.

In the orbital system, starting from the three points closest to the time of acquisition, the circumference parameters are computed; in a SpotLight image, the RMSE fit is at few meters level, mainly with respect to mean orbital plane.

Once the flight path has been determinated, the goal is to determine the satellite position for each line of the image according to the zero-Doppler geometry; to this aim a further time discretization along the satellite path is performed, in correspondence to the image acquisition. A single time interval from metadata was divided in ten parts, obtaining many satellite positions that describe the orbit (Figure 4.8).

These positions are transformed in the ECI system, then in the ECEF system and finally in the geodetic local system, in which the model Equations 4.29 are expressed.

In the geodetic local system the orbit has a complex shape due to rotation from ECI to ECEF to the local system. Nevethless due to the shortness of the orbital arc, again a circular model is adopted and a new circumference is estimated using the position in the local system. This simplified orbit is used in order to evaluate the satellite position related to image lines.

Starting from each GCP coordinates on the ground, we find the corresponding position, and consequently the velocity, that satisfies the zero-Doppler constrain (first Equation of 4.29) along the satellite orbit, that means velocity perpendicular to the line-of-sight (Figure 4.9).

In this way we can obtain a time of acquisition, a satellite position and velocity, for each GCP.

These times of acquisition are employed to estimate the parameters of the model, as described in the next section.

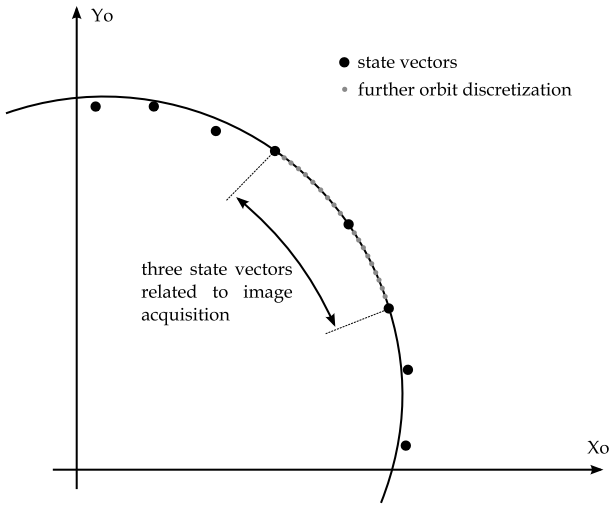

Figure 4.8: Orbital state vectors fitting with circumference

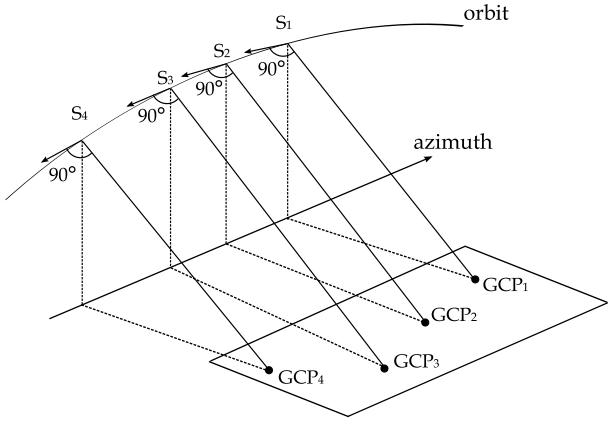

Figure 4.9: Satellite positions corresponding to the GCPs along the orbit according to zero-Doppler geometry

4.4.2 The concept of self-calibration parameters

The image coordinates I, J are related to the slant range R_s and to the time of acquisition t respectively. The parameters that establish the relation between image coordinates and "physical" parameters R_s and t can be considered as self-calibration parameters, since they provide a physical meaning to the image space.

The significance of the slant range R_s is clear from its definition: it represents the distance between the satellite and the target on the ground during the image acquisition. Its relation with the image coordinate I is:

$$R_s = D_s + \Delta r \cdot I \tag{4.30}$$

where the near range D_s is a calibration parameter related to the range measure, and the slant range resolution Δr is known from metadata; this parameter is calculated using the GCPs positions and their corresponding satellite positions, computed as described in Section 4.4.1, then in the least square process a refinement is obtained for it.

As regards the image coordinate J and the time t, their relationship can be expressed by a linear function (Figure 4.10), since the satellite angular velocity can be considered constant along the short orbital arc related to the SpotLight image acquisition:

$$t = k_{t0} + k_{t1} \cdot J \tag{4.31}$$

where the coefficients k_{t0} and k_{t1} are the calibration parameters; also in this case their approximate values are computed from the fitting of the times of GCPs acquisition, computed as described in Section 4.4.1, then a refinement is provided in the least square process.

The relation between the line J and the time t is crucial in order to estimate satellite position and velocity for a given point on the image.

Thus, the least squares solution of the orientation problem is devoted to the estimation of the three parameters D_s, k_{t0}, k_{t1} for each image.

4.4.3 The full stereo functional model

The functional model (for example, [31]) in short form reads: $f(y, x) = 0$ and its linearized form is $Ax + b = 0$. In this model the four radargrammetric equations F_1 and F_2 for the first image and F_3 and F_4 for the second image (see Equation 4.29) are written for each available GPs.

As usual the solution is obtained iteratively due to non-linearity of the system; the iterative procedure stops when the estimated variance of unit weight reaches a local minimum.

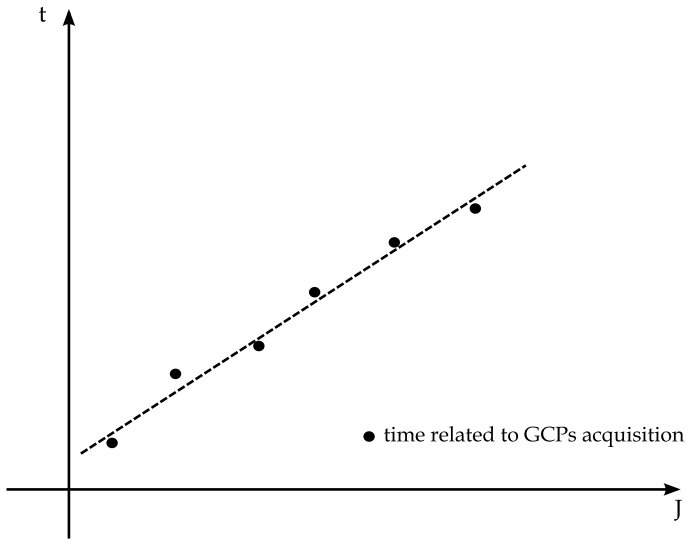

Figure 4.10: Fitting of GCPs times with linear function

Pseudo-observation on the GCPs are also allowed in the design matrix, in order to account for their accuracy, which may vary depending on their origin (cartography or direct surveys).

The pseudo-observation equations are provided for ground coordinates and for the image coordinate I and they are expressed in the following form:

$$\begin{cases} F_5 : \hat{X} = \tilde{X} + \delta X \\ F_6 : \hat{Y} = \tilde{Y} + \delta Y \\ F_7 : \hat{Z} = \tilde{Z} + \delta Z \\ F_8 : \hat{I} = \tilde{I} + \delta I \end{cases} \tag{4.32}$$

where the correction to ground and image coordinates $\delta X, \delta Y, \delta Z, \delta I$ are the unknown to be estimated, $\tilde{X}, \tilde{Y}, \tilde{Z}, \tilde{I}$ represent the approximate values of GCPs coordinates, and $\hat{X}, \hat{Y}, \hat{Z}, \hat{I}$ represent the corrected values of GCPs coordinates.

In the following model all the unknowns related to both images have to be estimated. If n is the number of GCPs, the relevant vectors and matrices can be sketched as follows:

x is the **vector of unknowns:**

$$x^T = \left| P^{(1)}, P^{(2)}, \ PO \ \right| \tag{4.33}$$

$$P^{(t)} = \left| k_{t0}^{(t)}, k_{t1}^{(t)}, D_s^{(t)} \right| \tag{4.34}$$

$$PO = \left| \delta X_1, \delta Y_1, \delta Z_1, \delta I_1^{(1)}, \delta I_1^{(2)}, \cdots \delta X_n, \delta Y_n, \delta Z_n, \delta I_n^{(1)}, \delta I_n^{(2)} \right| \tag{4.35}$$

where the superscript (t) is referred to the first or the second image and PO represents the correction of GCPs coordinates.

d is the **known vector:**

$$d = \left| \begin{array}{c} d_1^{(1)} \\ d_2^{(1)} \\ \vdots \\ d_n^{(1)} \\ d_1^{(2)} \\ d_2^{(2)} \\ \vdots \\ d_n^{(2)} \\ d_{p1} \\ d_{p2} \\ \vdots \\ d_{pn} \end{array} \right| \rightarrow for\ i^{th}\ GP \begin{cases} d_i^{(1)} = \left| \begin{array}{c} \tilde{F}_1 \\ \tilde{F}_2 \end{array} \right| \\ d_i^{(2)} = \left| \begin{array}{c} \tilde{F}_3 \\ \tilde{F}_4 \end{array} \right| \\ d_{pi} = \left| \begin{array}{c} \tilde{F}_5 \\ \tilde{F}_6 \\ \tilde{F}_7 \\ \tilde{F}_8^{(1)} \\ \tilde{F}_8^{(2)} \end{array} \right| \end{cases} \tag{4.36}$$

A is the **design matrix:**

$$\mathbf{A} = \begin{vmatrix} \mathbf{A}_1^{(1)} & \mathbf{A}_{p1}^{(1)} & 0 & 0 & 0 \\ \mathbf{A}_2^{(1)} & 0 & \mathbf{A}_{p2}^{(1)} & 0 & 0 \\ \vdots & 0 & 0 & \vdots & 0 \\ \mathbf{A}_n^{(1)} & 0 & 0 & 0 & \mathbf{A}_{pn}^{(1)} \\ \mathbf{A}_1^{(2)} & \mathbf{A}_{p1}^{(2)} & 0 & 0 & 0 \\ \mathbf{A}_2^{(2)} & 0 & \mathbf{A}_{p2}^{(2)} & 0 & 0 \\ \vdots & \vdots & \vdots & \vdots & \vdots \\ \mathbf{A}_n^{(2)} & 0 & 0 & 0 & \mathbf{A}_{pn}^{(2)} \\ 0 & 1 & & 0 & 0 \\ \vdots & & \ddots & & \vdots \\ 0 & 0 & & 1 & 0 \\ 0 & 0 & & 0 & 1 \end{vmatrix} \tag{4.37}$$

$$for\ i^{th}\ \ GP \rightarrow \begin{cases} \mathbf{A}_i^{(1)} = \begin{vmatrix} \partial_{k_{t0}^{(1)}} F_1 & \partial_{k_{t1}^{(1)}} F_1 & \partial_{D_s^{(1)}} F_1 & 0 & 0 & 0 \\ \partial_{k_{t0}^{(1)}} F_2 & \partial_{k_{t1}^{(1)}} F_2 & \partial_{D_s^{(1)}} F_2 & 0 & 0 & 0 \end{vmatrix} \\ \mathbf{A}_i^{(2)} = \begin{vmatrix} 0 & 0 & 0 & \partial_{k_{t0}^{(2)}} F_3 & \partial_{k_{t1}^{(2)}} F_3 & \partial_{D_s^{(2)}} F_3 \\ 0 & 0 & 0 & \partial_{k_{t0}^{(2)}} F_4 & \partial_{k_{t1}^{(2)}} F_4 & \partial_{D_s^{(2)}} F_4 \end{vmatrix} \end{cases}$$

$$for\ i^{th}\ \ GP \rightarrow \begin{cases} \mathbf{A}_{pi}^{(1)} = \begin{vmatrix} \partial_{X_i} F_1 & \partial_{Y_i} F_1 & \partial_{Z_i} F_1 & \partial_{I_i^{(1)}} F_1 & 0 \\ \partial_{X_i} F_2 & \partial_{Y_i} F_2 & \partial_{Z_i} F_2 & \partial_{I_i^{(2)}} F_2 & 0 \end{vmatrix} \\ \mathbf{A}_{pi}^{(2)} = \begin{vmatrix} \partial_{X_i} F_3 & \partial_{Y_i} F_3 & \partial_{Z_i} F_3 & 0 & \partial_{I_i^{(2)}} F_3 \\ \partial_{X_i} F_4 & \partial_{Y_i} F_4 & \partial_{Z_i} F_4 & 0 & \partial_{I_i^{(2)}} F_4 \end{vmatrix} \end{cases}$$

4.4.4 The stochastic model

The stochastic model is $\mathbf{C}_{YY} = \sigma_0^2 \mathbf{Q}$, where $\sigma_0^2 = 1$ (a priori choice) and the cofactor matrix $\mathbf{Q}$ is chosen diagonal both for the observations and pseudo-observation for the sake of simplicity, being usually hard to evaluate the correla-

tions:

$$\mathbf{C}_{YY} = \mathbf{Q} = \begin{vmatrix} \mathbf{C}_{1F_1F_2} & & 0 & & & & & & & \\ & \ddots & & & & & & & & \\ 0 & & \mathbf{C}_{nF_1F_2} & & & & & & & \\ & & & \mathbf{C}_{1F_3F_4} & & 0 & & & & \\ & & & & \ddots & & & & & \\ & & & 0 & & \mathbf{C}_{nF_3F_4} & & & & \\ & & & & & & \mathbf{C}_{1psd} & & 0 & \\ & & & & & & & \ddots & & \\ & & & & & & 0 & & \mathbf{C}_{npsd} & \end{vmatrix} \tag{4.38}$$

$$for\ i^{th}\ GCP \rightarrow \begin{cases} \mathbf{C}_{iF_1F_2} = \begin{vmatrix} \sigma^2_{F_1} & 0 \\ 0 & \sigma^2_{F_2} \end{vmatrix} \\ \mathbf{C}_{iF_3F_4} = \begin{vmatrix} \sigma^2_{F_3} & 0 \\ 0 & \sigma^2_{F_4} \end{vmatrix} \\ \mathbf{C}_{ipsd} = \begin{vmatrix} \sigma^2_{X_T} & \sigma_{X_T}\sigma_{Y_T} & \sigma_{X_T}\sigma_{Z_T} & 0 & 0 \\ \sigma_{Y_T}\sigma_{X_T} & \sigma^2_{Y_T} & \sigma_{Y_T}\sigma_{Z_T} & 0 & 0 \\ \sigma_{Z_T}\sigma_{X_T} & \sigma_{Z_T}\sigma_{Y_T} & \sigma^2_{Z_T} & 0 & 0 \\ 0 & 0 & 0 & \sigma_I^{(1)^2} & 0 \\ 0 & 0 & 0 & 0 & \sigma_I^{(2)^2} \end{vmatrix} \end{cases} \tag{4.39}$$

The standard deviation of the image observations is set equal to 1 pixel at least in radar images; for this kind of imagery a problem in GCPs acquisition is the pointing accuracy of natural targets and the GCPs location uncertainty can be estimated to be on the order of 1-3 pixels for such features [3].

For the GCP coordinates standard deviations are usually set equal to mean values obtained during their direct surveys or cartographic selection.

Chapter 5

RPC application and generation for SAR imagery

The Rational Polynomial Functions (RPFs) model with the employment of Rational Polynomial Coefficients (RPCs) is a well known method to orientate optical satellite imagery. In fact, some satellite imagery vendors have considered the use of RPFs models as a standard to supply a re-parametrized form of the sensor model in terms of the RPCs, secretly generated from their own physical sensor models.

Even if the rigorous models should theoretically provide the highest accuracy, they are only available for some satellites and can be managed by a few of commercially available software. Moreover, in order to estimate the unknown parameters of rigorous models, users are still faced with the challenging task of recovering the external orientation of the sensor using a set of GCPs usually no small than 10. When no or few GCPs are available, users cannot recover the external orientation of the sensor and therefore they are unable to perform various mapping and data collection operations.

With the introduction of generalized sensor models, this situation has changed considerably. Generalized sensor models, such as the RPFs [32], have smoothed the requirement to manage a physical sensor model. Furthermore, as the RPCs implicitly provide the interior and (approximate) external sensor orientation, the availability of several GCPs is no longer a mandatory requirement.

Consequently, the use of the RPCs for photogrammetric mapping became a new standard in high-resolution satellite imagery, that is adopted for all the

most important high and very high resolution sensors, such as Ikonos, QuickBird, WorldView-1 and GeoEye-1.

High resolution satellite imagery are now available in different formats and processing levels at an affordable price. These kinds of imagery and their growing availability are revolutionizing the role of satellite imagery in a number of applications ranging from intelligence to security, media, marketing, agriculture, utilities, urban planning, forestry, environmental monitoring, transportation etc.; in this sense, the users are not necessarily remote sensing experts, and they need a simple way to manage the data and the RPFs model represents a fundamental tool for exploiting the full geometrical potentiality of the imagery in a quite simple way.

Overall the simplicity of the RPFs model is due to three important reasons:

- the implementation of the RPFs model is standard, unique for all the sensors and much more simple that the one of a rigorous model, which have to be customized for each sensor
- the performances of the RPFs model, using a refinement transformation if it is needed, can reach the level of the ones from rigorous models
- the usage requires zero or, at maximum, quite few GCPs if refinement transformations are used, so that the cost for ancillary information is remarkably reduced with respect to rigorous models, which often require at least 10-12 GCPs for optical images or 5-6 for SAR images to supply a stable orientation

Therefore, the use of RPCs could be conveniently extended also to SAR imagery. Therefore, considering that only RadarSat-2 supplies imagery with RPCs file, the RPCs generation tool already implemented in SISAR for optical imagery has been extended to comply with COSMO-SkyMed and TerraSAR-X imagery.

5.1 RPCs Usage and Orientation Refinement

As mentioned before, some companies (for example DigitalGlobe for QuickBird and WorldView, Space Imaging for Ikonos and GeoEye-1, and the India Space Research Organization for Cartosat-1) usually supply the RPCs, as part of the image metadata to enable image orientation via RPFs.

The RPFs relate object point coordinates (latitude φ, longitude λ and height h) to pixel coordinates (I, J), in the form of ratios of polynomial expressions:

$$I = \frac{P_1(\varphi, \lambda, h)}{P_2(\varphi, \lambda, h)} \qquad J = \frac{P_3(\varphi, \lambda, h)}{P_4(\varphi, \lambda, h)} \tag{5.1}$$

where φ, λ are the geographic coordinates, h is the height above the WGS84 ellipsoid and (I, J) are the image coordinates. The order of these four polynomials is usually limited to 3 so that each polynomial takes the generic form:

$$P_n = \sum_{i=0}^{m_1} \sum_{j=0}^{m_2} \sum_{k=0}^{m_3} t_{ijk} \varphi^i \lambda^j h^k \tag{5.2}$$

with $0 \leq m_1 \leq 3$; $0 \leq m_2 \leq 3$; $0 \leq m_3 \leq 3$ and $m_1 + m_2 + m_3 \leq 3$, where t_{ijk} are the RPCs.

The number of RPCs depends obviously on the polynomial order: if the equations (5.1) are written with third order polynomials, the maximum number of coefficients is 80 (20 for each polynomial). Actually, the total number of RPCs is reduced to 78, because the two equations can be divided for the zero order terms of their denominators; so that the final form of the equations (5.1) reads:

$$\begin{aligned} I &= \frac{P_1(\varphi,\lambda,h)}{P_2(\varphi,\lambda,h)} = \frac{a_0+a_1\lambda+a_2\varphi+a_3h+a_4\lambda\varphi+\ldots+a_{17}\lambda^3+a_{18}\varphi^3+a_{19}h^3}{1+b_1\lambda+b_2\varphi+b_3h+b_4\lambda\varphi+\ldots+b_{17}\lambda^3+b_{18}\varphi^3+b_{19}h^3} \\ J &= \frac{P_3(\varphi,\lambda,h)}{P_4(\varphi,\lambda,h)} = \frac{c_0+c_1\lambda+c_2\varphi+c_3h+c_4\lambda\varphi+\ldots+c_{17}\lambda^3+c_{18}\varphi^3+c_{19}h^3}{1+d_1\lambda+d_2\varphi+d_3h+d_4\lambda\varphi+\ldots+d_{17}\lambda^3+d_{18}\varphi^3+d_{19}h^3} \end{aligned} \tag{5.3}$$

where now a_j, b_j, c_j, d_j are the RPCs.

The great power of these equations is the independence from the physical characteristic of the image acquisition [33]. Although ground coordinates are not directly connected with the acquisition physics, it is possible taking into account the further approximated considerations [34]: ratios of the first order terms can represent distortions caused by the optical projection, while corrections such as Earth curvature, atmospheric refraction and lens distortion can be well modeled by the second order terms; other unknown and more complex distortions with high order components may be absorbed by the third order terms.

The ground coordinates (φ, λ, h) and the image coordinates (I, J) in the equation (5.1) are normalized to the (-1, +1) range using normalization parameters supplied in the metadata file, in order to improve the numerical stability during the computation.

The generic simple formula utilized for the normalization, is:

$$T_N = \frac{T - T_{offset}}{T_{scale}} \tag{5.4}$$

where T_N are the normalized coordinates, T_{offset}, T_{scale} are the normalization parameters available in the metadata file and T is the original ground or image coordinate $(T = I, J; \varphi, \lambda, h)$.

Up to now, it is clear that the availability of all the coefficients a_j, b_j, c_j, d_j in the Equations 5.3 directly enables the external orientation and GCPs are

not necessary in theory. Nevertheless, since the residual bias may be present into the RPCs provided by the companies, the orientation can be refined on the basis of eventually known GPs, acting as GCPs. A possible refinement of the model (5.1) (written in normalized coordinates), allowing for bias compensation, is accomplished in a quite common way with the introduction of a simple first order polynomial in the RPFs (5.3) whose parameters are estimated, provided a suitable number of GCPs [35].

$$
\begin{aligned}
&I_N = A_0 + I_N \cdot A_1 + J_N \cdot A_2 + \frac{P_1(\varphi_N,\lambda_N,h_N)}{P_2(\varphi_N,\lambda_N,h_N)} = \\
&= A_0 + I_N \cdot A_1 + J_N \cdot A_2 + \frac{a_0+a_1\lambda_N+a_2\varphi_N+a_3h_N+a_4\lambda_N\varphi_N+\ldots+a_{17}\lambda_N^3+a_{18}\varphi_N^3+a_{19}h_N^3}{1+b_1\lambda_N+b_2\varphi_N+b_3h_N+b_4\lambda_N\varphi_N+\ldots+b_{17}\lambda_N^3+b_{18}\varphi_N^3+b_{19}h_N^3} \\
&J_N = B_0 + J_N \cdot B_1 + I_N \cdot B_2 + \frac{P_3(\varphi_N,\lambda_N,h_N)}{P_4(\varphi_N,\lambda_N,h_N)} = \\
&= B_0 + J_N \cdot B_1 + I_N \cdot B_2 + \frac{c_0+c_1\lambda_N+c_2\varphi_N+c_3h_N+c_4\lambda_N\varphi_N+\ldots+c_{17}\lambda_N^3+c_{18}\varphi_N^3+c_{19}h_N^3}{1+d_1\lambda_N+d_2\varphi_N+d_3h_N+d_4\lambda_N\varphi_N+\ldots+d_{17}\lambda_N^3+d_{18}\varphi_N^3+d_{19}h_N^3}
\end{aligned}
\tag{5.5}
$$

where (I_N, J_N) are the normalized images coordinates, and P_i are third order polynomial functions of object space normalized coordinates $(\varphi_N, \lambda_N, h_N)$; A_i and B_i terms describe image shift and drift effects (Figure 5.1). In particular:

- $A_0, A_1, A_2, B_0, B_1, B_2$ describe a complete affine transformation
- A_0, A_1, B_0, B_1 model the shift and drift
- A_0, B_0 describe a simple coordinate shift

The six new coefficients (A_i, B_i) are least squares estimated on the basis of the known GCPs. In theory the model is not linear, since the 2^{nd} and 3^{rd} terms of the right side involve both observations (I_N, J_N) and parameters (A_i, B_i); nevertheless, usually in the right side observations I_N, J_N may be considered as fixed coefficients, so that the model is treated as linear with respect to the six coefficients (A_i, B_i).

The formal structure of the functional model with full parametrization for the final estimation is the following, considering that n is the GCPs number:

$$y = \mathbf{A}x + l \tag{5.6}$$

where:

$\mathbf{A}$ is the **design matrix**

$$
\mathbf{A} = \left|\begin{array}{l|l} \mathbf{A}_1 & \rightarrow \ 1°\text{GCP} \\ \mathbf{A}_2 & \rightarrow \ 2°\text{GCP} \\ . & \\ \mathbf{A}_n & \rightarrow \ n°\text{GCP} \end{array}\right| \quad \text{for i}^{\text{th}}\ \text{GCP} \rightarrow \mathbf{A}_\text{i} = \left|\begin{array}{cccccc} 1 & I_N & J_N & 0 & 0 & 0 \\ 0 & 0 & 0 & 1 & J_N & I_N \end{array}\right|
\tag{5.7}
$$

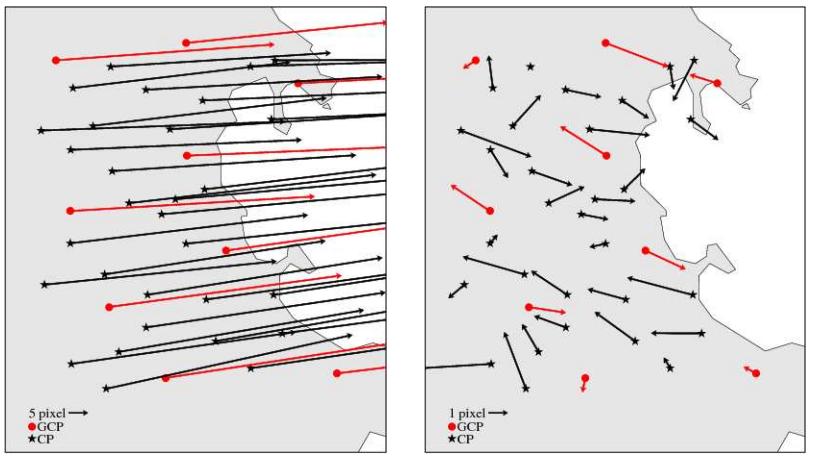

(a) (b)

Figure 5.1: Example of residuals adjustment with an affine transformation on a QuickBird image. Uncorrected (a) and corrected (b) image

l is the **known term**

$$l = \begin{vmatrix} l_1 \\ l_2 \\ . \\ l_n \end{vmatrix} \begin{matrix} \rightarrow & 1°\text{GCP} \\ \rightarrow & 2°\text{GCP} \\ & \\ \rightarrow & n°\text{GCP} \end{matrix} \quad \text{for i}^{\text{th}}\ \text{GCP} \rightarrow \text{l}_\text{i} = \begin{vmatrix} \frac{P_1(\varphi_{i_N},\lambda_{i_N},h_{i_N})}{P_2(\varphi_{i_N},\lambda_{i_N},h_{i_N})} \\ \frac{P_3(\varphi_{i_N},\lambda_{i_N},h_{i_N})}{P_4(\varphi_{i_N},\lambda_{i_N},h_{i_N})} \end{vmatrix} \tag{5.8}$$

y is the **observations vector**

$$y = \begin{vmatrix} y_1 \\ \vdots \\ y_i \\ \vdots \\ y_n \end{vmatrix} \quad \text{for i}^{\text{th}}\ \text{GCP} \quad \rightarrow \quad y_i = \begin{vmatrix} I_N \\ J_N \end{vmatrix} \tag{5.9}$$

x is the **unknown vector**

$$x^T = |A_0, A_1, A_2, B_0, B_1, B_2| \tag{5.10}$$

As regards the stochastic model, an unit identity diagonal cofactor matrix for observation (I, J) is assumed.

5.2 RPCs Generation

The RPCs can be generated by a terrain-dependent scenario without using any physical sensor model [36] or according to a terrain-independent scenario, using a known physical sensor model.

For the terrain-dependent scenario, which is a kind of registration of the original image to 3D geometry represented by the GCPs, the RPFs model tries to approximate the complicated imaging geometry across the image scene using polynomial terms.

The solution is highly dependent on the actual terrain relief, the distribution and the number of GCPs. The RPCs have to be estimated in a least squares adjustment so that the number of GCPs could be very high (at least 39 if RPCs up to the third order are looked for). This method is very weak and vulnerable in presence of outliers and it is likely to cause deformations far from the GCPs returning not good accuracies.

Therefore, the RPFs solved by terrain-dependent approach must not be used as a replacement sensor model if high accuracy is required [36], [37], [38] and will not be considered anymore hereafter.

5.2.1 RPCs generation with a terrain-independent scenario

The RPCs generation, following a terrain-independent scenario, starts from the definition of a 2D image grid covering the full extent of the image and its corresponding 3D object grid with several layers (e.g., four or more layers for the third-order case) slicing the entire elevation range of the terrain.

The horizontal coordinates in a local system $(North, East)$ of a point of the 3D object grid are calculated from a point (I, J) of the image grid using the physical sensor model with an a priori selected elevation h. Then, the RPCs are least squares estimated with all object grid points and the image grid points. This terrain-independent computational scenario can make the RPFs model a good replacement to the physical sensor models, and has been widely used to determine the RPCs.

It has to be underlined that in the usually adopted terrain-independent approach, the least squares solution is often carried out through a regularization, since unknown RPCs may be highly correlated so that the design matrix is almost rank deficient [39].

In order to overcome the regularization requirements, an innovative algorithm for the RPCs extraction with a terrain independent approach was defined

and implemented in SISAR. As mentioned above, at first an image discretization is made, dividing the full extent image space in a 2D grid. Then, the points of the 2D image grid are used to generate the 3D ground grid: the image was oriented and the SISAR rigorous model is used to create the 3D grid, starting from each point of the 2D grid image. In this respect, it has to be underlined that the 2D grid is actually a regular grid, whereas the 3D one is not strictly regular, due to the image deformations.

Moreover, the 3D grid points were generated intersecting the line of sight of the satellite modeled by the rigorous model equations with surfaces (approximately ellipsoids) concentric to the WGS84 ellipsoid, placed at regular elevation steps. So, the dimension of the 3D grid is both based on the full extent of the image and the elevation range of the terrain [40].

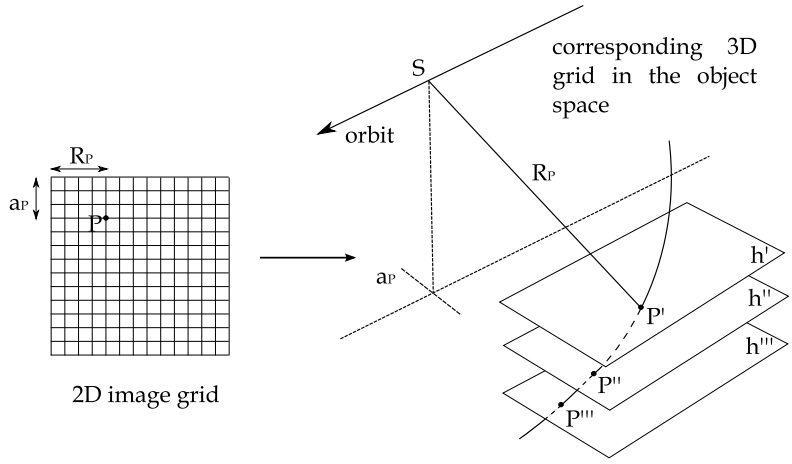

Figure 5.2: Grid for RPCs generation in the terrain-independent approach

The 3D grid contains several elevation layers uniformly distributed, and the points on one layer have the same elevation value (Figure 5.2).

Note that the finest subdivision depends on the incompressible error of the rigorous model used to generate the RPCs, so that a very fine discretization is not useful and therefore an upper discretization reasonable limit exists. The RPCs least squares estimation [37] is based on the linearization of the generic RPFs equations, which can be written as:

$$\begin{aligned} &I_N + b_1\lambda_N I_N + b_2\varphi_N I_N + ... + b_{19}h_N^3 I_N - a_0 - a_1\lambda_N - a_2\varphi_N ... - a_{19}h_N^3 = 0 \\ &J_N + d_1\lambda_N J_N + d_2\varphi_N J_N + ... + d_{19}h_N^3 J_N - c_0 - c_1\lambda_N - c_2\varphi_N ... - c_{19}h_N^3 = 0 \end{aligned} \tag{5.11}$$

where a_i, b_i, c_i, d_i are the RPCs (78 coefficients for third order polynomials), (I_N, J_N) and $(\varphi_N, \lambda_N, h_N)$ are the normalized coordinates obtained throughout the equation (5.4), with scale and offset factors computed according to:

$$\begin{cases} w_{offset} = \min(w_k) \\ w_{scale} = \max(w_k) - \min(w_k) \\ I_{offset} = J_{offset} = 1 \\ I_{scale} = n°column - 1 \\ J_{scale} = n°row - 1 \end{cases} \text{where} \quad w = \varphi_N, \lambda_N, h_N \tag{5.12}$$

where k is the number of available GCPs and $n°column/row$ are the total columns/rows number of the image; the normalization range is (0, 1).

Since the equations (5.11) are completely independent, the least squares estimation may be performed separately for the two image coordinates (I_N, J_N):

$$\begin{aligned} &\mathbf{A}_I x_I + y_I = 0 \\ &\mathbf{A}_J x_J + y_J = 0 \end{aligned} \tag{5.13}$$

where $\mathbf{A}_I$, $\mathbf{A}_J$ are the design matrices (depending on the image and ground coordinates at the chosen different layers), x_I ,x_J are the unknown parameters (RPCs) and y_I,y_J are the known terms (image coordinates):

$$\mathbf{A}_I = \begin{vmatrix} \mathbf{A}_{I,1} \\ \mathbf{A}_{I,2} \\ \vdots \\ \mathbf{A}_{I,n} \end{vmatrix} \begin{vmatrix} \rightarrow \\ \rightarrow \\ \\ \rightarrow \end{vmatrix} \begin{matrix} 1°\text{GCP} \\ 2°\text{GCP} \\ \\ n°\text{GCP} \end{matrix} \quad x_I = \begin{vmatrix} a_0 \\ a_1 \\ a_2 \\ \vdots \\ a_{19} \\ b_1 \\ b_2 \\ b_3 \\ \vdots \\ b_{19} \end{vmatrix} \quad y_I = \begin{vmatrix} I_{N,1} \\ I_{N,2} \\ \vdots \\ I_{N,n} \end{vmatrix} \begin{vmatrix} \rightarrow \\ \rightarrow \\ \\ \rightarrow \end{vmatrix} \begin{matrix} 1°\text{GCP} \\ 2°\text{GCP} \\ \\ n°\text{GCP} \end{matrix} \tag{5.14}$$

for a generic GCP i the design matrix row $\mathbf{A}_{I,i}$ has form that is:

$$\begin{array}{c}\mathbf{A}_{I,i} = |I_N\varphi_N \quad I_N\lambda_N \quad I_N h_N \quad \cdots \quad I_N\varphi_N^3 \quad I_N\lambda_N^3 \quad I_N h_N^3 \quad -1 \\ -\varphi_N \quad -\lambda_N \quad -h_N \quad \cdots \quad -\varphi_N^3 \quad -\lambda_N^3 \quad -h_N^3\ |\end{array} \tag{5.15}$$

$$\mathbf{A}_J = \left|\begin{array}{c|cl} \mathbf{A}_{J,1} & \rightarrow & 1°\text{GCP} \\ \mathbf{A}_{J,2} & \rightarrow & 2°\text{GCP} \\ \vdots & & \\ \mathbf{A}_{J,n} & \rightarrow & n°\text{GCP} \end{array}\right| \quad x_J = \left|\begin{array}{c} c_0 \\ c_1 \\ c_2 \\ \vdots \\ c_{19} \\ d_1 \\ d_2 \\ d_3 \\ \vdots \\ d_{19} \end{array}\right| \quad y_J = \left|\begin{array}{c|cl} J_{N,1} & \rightarrow & 1°\text{GCP} \\ J_{N,2} & \rightarrow & 2°\text{GCP} \\ \vdots & & \\ J_{N,n} & \rightarrow & n°\text{GCP} \end{array}\right| \tag{5.16}$$

for a generic GCP i the design matrices row $\mathbf{A}_{J,i}$ has the form that is:

$$\begin{array}{c}\mathbf{A}_{J,i} = |J_N\varphi_N \quad J_N\lambda_N \quad J_N h_N \quad \cdots \quad J_N\varphi_N^3 \quad J_N\lambda_N^3 \quad J_N h_N^3 \quad -1 \\ -\varphi_N \quad -\lambda_N \quad -h_N \quad \cdots \quad -\varphi_N^3 \quad -\lambda_N^3 \quad -h_N^3\ |\end{array} \tag{5.17}$$

Deeper investigations underlined that many RPCs are highly correlated. In order to avoid instability due to high correlations, leading to a pseudo-singular design matrix, Tickhonov regularization is usually used. Generally, the regularization is exploited in a Tickhonov fashion, adopting a damping factor to the diagonal of the normal matrix, in order to guarantee its non singularity.

A new alternative approach is based on the Singular Value Decomposition (SVD) and QR decomposition, which are employed to evaluate the actual rank of the design matrix and to select the actual estimable coefficients [41], [40].

The Singular Value Decomposition (SVD) is a very powerful technique to deal with sets of equations or matrices that are either singular or numerically very close to being singular. The SVD of a matrix $\mathbf{A} \in \Re^{m\times n}$ (with $m \geq n$) is any factorization of the form:

$$\mathbf{A} = \mathbf{U}\mathbf{W}\mathbf{V}^{\mathrm{T}} \tag{5.18}$$

where $\mathbf{W} \in \Re^{n\times n}$ is a diagonal matrix with positive or zero elements (w_{ij}) that are the singular values of $\mathbf{A}$; $\mathbf{U} \in \Re^{m\times n}$ and $\mathbf{V} \in \Re^{n\times n}$ are orthogonal matrices, whose columns (u_j, v_j) are called the left and right singular vectors. For a system

of linear equations ($\mathbf{A}\boldsymbol{x} = \boldsymbol{b}$), using the SVD we can write ([42], chapter 5.5.3):

$$\mathbf{UWV}^{\mathrm{T}}\mathbf{x} = \mathbf{b} \tag{5.19}$$

and the LS solution $\boldsymbol{x}$ minimizes $||\mathbf{A}\boldsymbol{x} - \boldsymbol{b}||_2$.

Since the orthogonal matrix preserves the norm, for any $\boldsymbol{x} \in \Re^n$ we have:

$$\|\mathbf{A}\boldsymbol{x} - \boldsymbol{b}\|_2^2 = \left\|(\mathbf{U}^{\mathrm{T}}\mathbf{AV})(\mathbf{V}^{\mathrm{T}}\boldsymbol{x}) - \mathbf{U}^{\mathrm{T}}\boldsymbol{b}\right\|_2^2 = \sum\nolimits_{i=1}^{r}(w_{ii}z_i - u_i^{\mathrm{T}}\boldsymbol{b})^2 + \sum\nolimits_{i=r+1}^{m}(u_i^{\mathrm{T}}\boldsymbol{b})^2 \tag{5.20}$$

where z_i is the i^{th} element of the vector $\boldsymbol{z} = \mathbf{V}^{\mathrm{T}}\boldsymbol{x}$ and r is the rank of $\mathbf{A}$. Of course $||\mathbf{A}\boldsymbol{x} - \boldsymbol{b}||_2^2 = minimum$ if

$$\sum_{i=1}^{r}(w_{ii}z_i - u_i^{\mathrm{T}}\boldsymbol{b})^2 = 0 \tag{5.21}$$

then using the SVD, the LS problem is now in form of a diagonal matrix, and finally

$$\begin{cases} x_i = \frac{u_i^{\mathrm{T}}\boldsymbol{b}}{w_{ii}}v_i & \text{if} \quad w_{ii} \neq 0 \\ x_i = \text{anything} & \text{if} \quad w_{ii} = 0 \end{cases} \tag{5.22}$$

The advantage of using the SVD is that it can reliably handle the rank deficient case as well as the full rank case.

The QR decomposition of a matrix $\mathbf{A} \in \Re^{m\times n}$ (with $m \geq n$) is given by:

$$\mathbf{A} = \mathbf{QR} \tag{5.23}$$

where $\mathbf{Q} \in \Re^{m\times m}$ an orthogonal matrix and $\mathbf{R} \in \Re^{m\times n}$ is an upper triangular matrix. If the rank of $\mathbf{A}$ is equal to n, the first n columns of $\mathbf{Q}$ form an orthonormal basis for the Range($\mathbf{A}$). Thus, the calculation of the QR factorization is a way to compute an orthonormal basis for a set of vectors. The standard algorithm for the QR decomposition involves sequential evaluation of Householder transformations. An appropriate Householder matrix, applied to a given matrix, can zero all the elements, situated below a given element, in a column of the matrix. For the first column of matrix $\mathbf{A}$ an appropriate matrix $\mathbf{H}_1$ is evaluated, which sets to zero all the elements below the first element in the first column of $\mathbf{A}$. Similarly $\mathbf{H}_2$ zeroes all elements in the second column below the second element and so on up to $\mathbf{H}_{n-1}$

$$\mathbf{R} = \mathbf{H}_{n-1}\cdots\mathbf{H}_1\mathbf{A} \tag{5.24}$$

where $\mathbf{Q}^{\mathrm{T}} = \mathbf{H}_{n-1}.....\mathbf{H}_1$, i.e. $\mathbf{Q} = \mathbf{H}_1.....\mathbf{H}_{n-1}$. The generic matrix $\mathbf{H}_i$

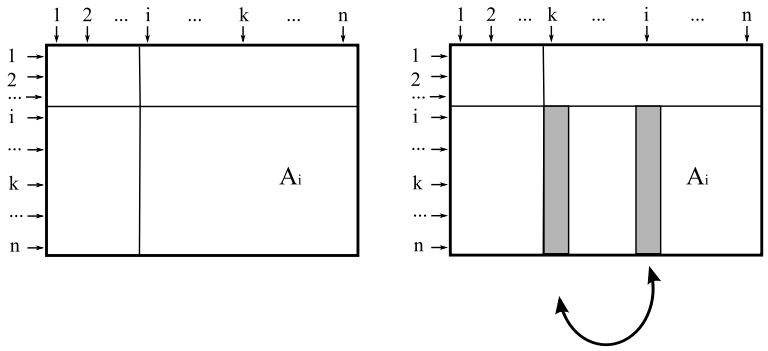

Figure 5.3: $\mathbf{A}_i$ before and after the permutation

zeroes all elements in the first column below the first element for a sub-matrix of $\mathbf{A}$ ($\mathbf{A}_i \in \Re^{(m-i)\times(n-i)}$). If $\mathbf{A}$ is rank deficient, the QR factorization does not give a basis for the Range($\mathbf{A}$). In this case to calculate an orthonormal basis for Range($\mathbf{A}$) it is necessary to compute the QR decomposition of a column-permuted version of $\mathbf{A}$, i.e. $\mathbf{AP} = \mathbf{QR}$ ([42], chapter 5.4)

$$\mathbf{Q}^{\mathrm{T}}\mathbf{AP} = \begin{bmatrix} \mathbf{R}_{11} & \mathbf{R}_{12} \\ 0 & 0 \\ \downarrow & \downarrow \\ r & n-r \end{bmatrix} \begin{matrix} \rightarrow \\ \rightarrow \\ \\ \end{matrix} \begin{matrix} r \\ m-r \\ \\ \end{matrix} \tag{5.25}$$

where $\mathbf{P}$ is a permutation, r is the rank of $\mathbf{A}$, $\mathbf{R}_{11}$ is an upper triangular and non singular matrix and $\mathbf{Q}$ and $\mathbf{P}$ are products of Householder matrices $\mathbf{Q} = \mathbf{H}_1 \ldots \mathbf{H}_r$, $\mathbf{P} = \mathbf{P}_1 \ldots \mathbf{P}_r$. For understanding the permutation matrix role it is necessary to define the vector $\boldsymbol{N} \in \Re^m$ for a generic matrix $\mathbf{A} \in \Re^{(m\times n)}$:

$$\mathbf{A}_{m,n} = \begin{vmatrix} a_{11} & a_{12} & \cdots & a_{1n} \\ a_{21} & a_{22} & \cdots & a_{2n} \\ \vdots & \cdots & & \vdots \\ a_{m1} & & \cdots & a_{mn} \end{vmatrix} \tag{5.26}$$

$$\boldsymbol{N}_m = \begin{vmatrix} \sum_{k=1}^{m} a_{k1}^2 & \sum_{k=1}^{m} a_{k2}^2 & \cdots & \sum_{k=1}^{m} a_{kn}^2 \end{vmatrix} \tag{5.27}$$

The element of the $\boldsymbol{N}$ are the square value of norm calculated for each column of $\mathbf{A}$. The permutation matrix $\mathbf{P}$ applied at the generic matrix $\mathbf{A}$ makes a matrix $\mathbf{A}_{\mathrm{P}} = \mathbf{AP}$ such that the elements of the corresponding vector $\boldsymbol{N}$ are

placed in decreasing order. As for the generic matrix $\mathbf{H}_i$, the generic matrix $\mathbf{P}_i$ permutes the column of a sub-matrix of $\mathbf{A}_i \in \Re^{(m-i)\times(n-i)}$ (Figure 5.3, left); if k is the column with the maximum value of norm, the permutation matrix $\mathbf{P}_i$ exchanges the columns i and k (Figure 5.3, right).

In a system of linear equations ($\mathbf{A}\boldsymbol{x} = \boldsymbol{b}$), if $\mathbf{A} \in \Re^{(m\times n)}$ and has a rank r, the QR decomposition produces the factorization $\mathbf{AP} = \mathbf{QR}$ where $\mathbf{R}$ is described in the equation (5.25). As for the LS problem we have:

$$\|\mathbf{A}\boldsymbol{x} - \boldsymbol{b}\|_2^2 = \left\|(\mathbf{Q}^{\mathrm{T}}\mathbf{AP})(\mathbf{P}^{\mathrm{T}}\boldsymbol{x}) - \mathbf{Q}^{\mathrm{T}}\boldsymbol{b}\right\|_2^2 = \|\mathbf{R}_{11}\boldsymbol{t} - (\boldsymbol{c} - \mathbf{R}_{12}\boldsymbol{z})\|_2^2 + \|\boldsymbol{d}\|_2^2 \tag{5.28}$$

Where

$$\mathbf{P}^{\mathrm{T}}\boldsymbol{x} = \begin{bmatrix} \boldsymbol{t} \\ \boldsymbol{z} \end{bmatrix} \begin{matrix} \rightarrow & r \\ \rightarrow & n-r \end{matrix} \tag{5.29a}$$

$\boldsymbol{t}$ is the vector that represents the first r rows of $\mathbf{P}^{\mathrm{T}}\boldsymbol{x}$, $\boldsymbol{z}$ is the vector that represents the remaining $n - r$ rows of the same vector.

$$\mathbf{Q}^{\mathrm{T}}\boldsymbol{b} = \begin{bmatrix} \boldsymbol{c} \\ \boldsymbol{d} \end{bmatrix} \begin{matrix} \rightarrow & r \\ \rightarrow & m-r \end{matrix} \tag{5.29b}$$

$\boldsymbol{c}$ is the vector that represents the first r rows of $\mathbf{Q}^{\mathrm{T}}\boldsymbol{b}$, $\boldsymbol{d}$ is the vector that represents the remaining $m - r$ rows of the same vector.

If $\boldsymbol{x}$ is a LS minimizer we have

$$\boldsymbol{x} = \mathbf{P}\begin{bmatrix} \mathbf{R}_{11}^{-1}(\boldsymbol{c} - \mathbf{R}_{12}\boldsymbol{z}) \\ \boldsymbol{z} \end{bmatrix} \tag{5.30}$$

If $\boldsymbol{z}$ is a set of zeroes in this expression, we obtain the basic solution:

$$\boldsymbol{x}_{\mathrm{B}} = \mathbf{P}\begin{bmatrix} \mathbf{R}_{11}^{-1}\boldsymbol{c} \\ 0 \end{bmatrix} \tag{5.31}$$

$\boldsymbol{x}_{\mathrm{B}}$ has at most r non-zero components and so $\mathbf{A}\boldsymbol{x}_{\mathrm{B}}$ involves a subset of $\mathbf{A}$ columns.

And finally the subset selection using the SVD and QR: for a system of linear equations ($\mathbf{A}\boldsymbol{x} = \boldsymbol{b}$), with $\mathbf{A} \in \Re^{(m\times n)}$ (with $m \geq n$) it is necessary to select the parameters that can be estimated. We describe an SVD-based subset selection procedure, due to Golub, Klema and Stewart ([42], chapter 12.2), that proceeds as follows:

- we compute the SVD $\mathbf{A} = \mathbf{UWV}^{\mathrm{T}}$ and use it to determine a rank estimate r
- with the QR decomposition $\mathbf{QR} = \mathbf{AP}$ we select an independent subset of

$\mathbf{A}$ columns; if $\mathbf{R}_{11}\boldsymbol{x}_{\mathrm{B}} = \mathbf{Q}^{\mathrm{T}}\boldsymbol{b}$ with $\boldsymbol{x}_{\mathrm{B}} \in \Re^r$ and we set:

$$\boldsymbol{t} = \mathbf{P}\begin{bmatrix} \boldsymbol{x}_{\mathrm{B}} \\ 0 \end{bmatrix} \tag{5.32}$$

then $\mathbf{A}\boldsymbol{t}$ is an approximate LS predictor of $\boldsymbol{b}$ that involves the first r columns of $\mathbf{AP}$. The permutation matrix $\mathbf{P}$ is calculated so that the columns of the matrix $\mathbf{B}_1 \in \Re^{(m\times r)}$ in $\mathbf{AP} = [\mathbf{B}_1, \mathbf{B}_2]$ are "sufficiently independent"

- we predict $\boldsymbol{b}$ with the vector $\mathbf{A}\boldsymbol{t}$ where $\boldsymbol{t}$ is described in the equation (5.32), and $\boldsymbol{z}$ minimizes $||\mathbf{B}_1\boldsymbol{x}_{\mathrm{B}} - \boldsymbol{b}||_2$

Moreover, the statistical significance of each estimable coefficient is checked by a Student T-test, so to avoid overparametrization; in case of not statistically significant coefficient, it is removed and the estimation process is repeated until all coefficients are significant. In most of the cases the "degrees of freedom" are high (more than 100), thus there could be considered infinite, converting the Student-T distribution in a normal standard distribution.

5.3 Stereo Model via RPCs

RPF model represents an attractive tool also for managing stereo pairs orientation and possible subsequent DSM generation.

The first problem to face with it is the computation of the approximate coordinates of Tie Points (TPs) on the ground (φ, λ, h), to initialize the linearization of the observation equations used for their least squares estimation. Tie Points are points automatically detected on both images of the stereo pair through a suited matching procedure, whose image coordinates are known and ground coordinates have to be estimated in order to generate a 3D terrain model.

In this case, a simple procedure may be followed, starting from the geolocation information available in the metadata file.

The geographic coordinate of the four corner of the image are known from the metadata ancillary data; these coordinate are transformed in the cartographic plane, where a 2-D affine transformation is estimated, in order to link the image coordinates to ground coordinate in a very raw way; the mean height of the area, also known from the metadata, is assigned to approximate coordinates. This raw transformation is enough to obtain approximate coordinates, that are then transformed into ellipsoidal ones.

A similar and more accurate procedure is the estimation of the 2-D affine parameters using the GCPs coordinates, when thay are available, in the place of the corner coordinates.

The approximate TPs are refined using the RPCs corrected with affine transformation. At first, the affine parameters (6 for each images) are estimated through the equations (5.5) (two for each image), established for each available GCP.

The functional model ($y = \mathbf{R}x + l$) for the estimation of affine parameters is the following:

$\mathbf{R}$ is the **design matrix**

$$\mathbf{R} = \left| \begin{array}{l|ll} \mathbf{R}^{(1)} & \rightarrow & \text{first image} \\ \mathbf{R}^{(2)} & \rightarrow & \text{second image} \end{array} \right| \qquad \mathbf{R}^{(t)} = \left| \begin{array}{l|ll} \mathbf{R}_1^{(t)} & \rightarrow & 1°\text{GCP} \\ \mathbf{R}_2^{(t)} & \rightarrow & 2°\text{GCP} \\ \vdots & & \\ \mathbf{R}_n^{(t)} & \rightarrow & n°\text{GCP} \end{array} \right|$$

$$\text{for i}^{\text{th}}\text{ GCP} \rightarrow \begin{cases} \mathbf{R}_i^{(1)} = \left| \begin{array}{cccccccccc} 1 & I_{N_i}^{(1)} & J_{N_i}^{(1)} & 0 & 0 & 0 & 0 & \cdots & 0 \\ 0 & 0 & 0 & 1 & I_{N_i}^{(1)} & J_{N_i}^{(1)} & 0 & \cdots & 0 \end{array} \right| \\ \mathbf{R}_i^{(2)} = \left| \begin{array}{cccccccccc} 0 & \cdots & 0 & 1 & I_{N_i}^{(2)} & J_{N_i}^{(2)} & 0 & 0 & 0 \\ 0 & \cdots & 0 & 0 & 0 & 0 & 1 & I_{N_i}^{(2)} & J_{N_i}^{(2)} \end{array} \right| \end{cases} \tag{5.33}$$

x is the **unknown vector**

$$x^T = \left| \begin{array}{cccccccccccc} A_0^{(1)} & A_1^{(1)} & A_2^{(1)} & B_0^{(1)} & B_1^{(1)} & B_2^{(1)} & A_0^{(2)} & A_1^{(2)} & A_2^{(2)} & B_0^{(2)} & B_1^{(2)} & B_2^{(2)} \end{array} \right| \tag{5.34}$$

l is the **known vector**

$$l = \left| \begin{array}{l|ll} l^{(1)} & \rightarrow & \text{first image} \\ l^{(2)} & \rightarrow & \text{second image} \end{array} \right|$$

$$l^{(t)} = \left| \begin{array}{l|ll} l_1^{(t)} & \rightarrow & 1°\text{GCP} \\ l_2^{(t)} & \rightarrow & 2°\text{GCP} \\ . & & \\ l_n^{(t)} & \rightarrow & n°\text{GCP} \end{array} \right| \quad \text{for i}^{\text{th}}\text{ GCP} \rightarrow \text{l}_\text{i} = \left| \begin{array}{l} \frac{P_1(\varphi_i,\lambda_i,h_i)}{P_2(\varphi_i,\lambda_i,h_i)} \\ \frac{P_3(\varphi_i,\lambda_i,h_i)}{P_4(\varphi_i,\lambda_i,h_i)} \end{array} \right| \tag{5.35}$$

y is the **observations vector**

$$y = \left| \begin{array}{l} y^{(1)} \\ y^{(2)} \end{array} \right| \begin{array}{ll} \rightarrow & \text{first image} \\ \rightarrow & \text{second image} \end{array} \qquad y^{(t)} = \left| \begin{array}{l} I_{N_1}^{(t)} \\ J_{N_1}^{(t)} \\ I_{N_2}^{(t)} \\ J_{N_2}^{(t)} \\ \vdots \\ I_{N_n}^{(t)} \\ J_{N_n}^{(t)} \end{array} \right| \begin{array}{l} \\ \rightarrow 1°\text{GCP} \\ \\ \rightarrow 2°\text{GCP} \\ \\ \\ \rightarrow n°\text{GCP} \\ \end{array} \tag{5.36}$$

where the superscripts (t) is related to the first or the second image; A_i, B_i are the affine parameters, (I_N, J_N) are the normalized image coordinates and P_i is correlated to equation (5.2).

Then, the refined RPCs model (5.5) is applied to each TP.

The functional model for the TPs ground coordinates estimation reads: y=$\mathbf{A}x$+l, where:

$\mathbf{A}$ is the **design matrix**

$$\mathbf{A} = \left| \begin{array}{ccc} \partial\left(I_N^{(1)}\right)/\partial\lambda & \partial\left(I_N^{(1)}\right)/\partial\varphi & \partial\left(I_N^{(1)}\right)/\partial h \\ \partial\left(J_N^{(1)}\right)/\partial\lambda & \partial\left(J_N^{(1)}\right)/\partial\varphi & \partial\left(J_N^{(1)}\right)/\partial h \\ \partial\left(I_N^{(2)}\right)/\partial\lambda & \partial\left(I_N^{(2)}\right)/\partial\varphi & \partial\left(I_N^{(2)}\right)/\partial h \\ \partial\left(J_N^{(2)}\right)/\partial\lambda & \partial\left(J_N^{(2)}\right)/\partial\varphi & \partial\left(J_N^{(2)}\right)/\partial h \end{array} \right| \tag{5.37}$$

x, l and y are the **unknown**, the **known** and the **observations vectors**

$$x^T = \left| \begin{array}{cccc} \varphi & \lambda & h \end{array} \right| \quad l = \left| \begin{array}{l} P_1^{(1)}(\varphi,\lambda,h)\Big/P_2^{(1)}(\varphi,\lambda,h) \\ P_3^{(1)}(\varphi,\lambda,h)\Big/P_4^{(1)}(\varphi,\lambda,h) \\ P_1^{(2)}(\varphi,\lambda,h)\Big/P_2^{(2)}(\varphi,\lambda,h) \\ P_3^{(2)}(\varphi,\lambda,h)\Big/P_4^{(2)}(\varphi,\lambda,h) \end{array} \right| \quad y = \left| \begin{array}{l} I_N^{(1)} \\ J_N^{(1)} \\ I_N^{(2)} \\ J_N^{(2)} \end{array} \right| \tag{5.38}$$

It has to be underlined that for the sake of completeness in the previous sections the general formulation of the affine RPCs refinement has been explained; this last refinement is not always necessary in order to achieve the best accuracy.

In fact, very often the RPCs provided together the optical imagery are affected by a systematic error that could be easily removed estimating the RPCs

affine adjustement, whereas in some cases, specially for the imagery projected on to ellipsoid (as IKONOS or QuickBird/WorldView Standard Orthoready imagery), only the simple shift refinement is significant and has to be applied. The significance of the refinement parameters has always to be evaluated by a significance test, as Student T-test.

In a least square problem $\hat{x}$ is the vector of estimable parameters and $\mathbf{C}_{\hat{x}\hat{x}}$ is the correspondent covariance matrix. Empiric value T_0 can be calculated dividing the estimated value $\hat{x}_i$ by its standard deviation $\sigma_{\hat{x}_i}$. T_0 must be compared with a critic value T_α of Student T-distribution with $m-n$ degrees of freedom, where n is the unknowns number, m is the equations number and α is the level of significance; if $T_0 > T_\alpha$ the parameter is considered significant.

As regards the RPCs generated using a terrain-independent approach, they are calibrated on accurate GCPs, and they are not affected by biases, therefore refinement transformation is not needed in this case.

In the results paragraphs, examples of the RPCs refinement and evaluation of affine parameters significance are shown and discussed.

Chapter 6

Radargrammetric model and RPCs generation results

6.1 Cosmo-SkyMED

COSMO-SkyMed (COnstellation of small Satellites for Mediterranean basin Observation) is the largest Italian investment in Space Systems for Earth Observation, commissioned and funded by Italian Space Agency (ASI) and Italian Ministry of Defense (MoD).

It has been created for a Dual-Use (Civilian and Defence), and it is actually a cutting edge system in the world in the Earth Observation field.

The system consists of a constellation of four Low Earth Orbit mid-sized satellites, each equipped with a multi-mode high-resolution Synthetic Aperture Radar (SAR) operating at X-band (Figure 6.1).

The fourth satellite has been launched on November 6, 2010; it is the last component of the mission, that is now finally fully operational.

The main goals of COSMO-SkyMed are related to a space mission having a dual nature (i.e. capable to satisfy civilian and defence customers) able to provide information and services to a number of activities and applications (such as risk management applications, cartography and planning applications, agriculture, forest, hydrology, geology, marine domain, archaeology, etc... [43]).

The capability of acquisition in every weather and illumination condition,

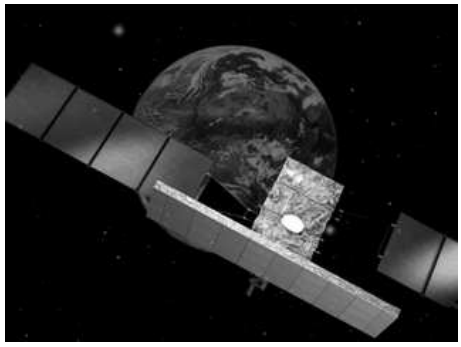

Figure 6.1: COSMO-SkyMed satellite by ASI

and of acquisition at regular short time intervals, makes COSMO-SkyMed suited to territory monitoring, to environmental planning and to emergency managing.

The set of requirements, imposed at highest level, has brought to the following needed performances:

- large amount of daily acquired images
- satellites worldwide accessibility
- all weather and day/night acquisition capabilities
- very fine image quality (e.g. spatial and radiometric resolution)
- possibility of image spatial resolution trade-off with size, at most possible extent and including sub-meter resolution

The orbit characteristics are summarized in the Table 6.1. The Tandem interferometric configurations is supported, in which the two satellites fly in close proximity achieving the acquisitions with a temporal gap of 24 hours. In this case the coherence problem may be only attenuated but not totally solved as for the TerraSAR-X TanDEM mission (see section 6.2).

COSMO-SkyMed is able to operate in three different acquisition mode:

- **SpotLight Mode:** the antenna is steered during the acquisition time in order to illuminate the required scene for a time period longer than the one of the standard strip side view, increasing the length of the synthetic antenna and therefore the azimuth resolution (at expense of the azimuth coverage).

Table 6.1: COSMO-SkyMed orbit characteristics

Orbit Type	SSO
Inclination	97.86°
Revolutions/day	14.8125
Orbit Cycle	16 days
Eccentricity	0.00118
Argument of Perigee	90°
Semi Major Axis	7003.52 km
Nominal Height	619.6 km
Local Time Ascending Node	6:00 A.M.
Number of Satellites	4
Phasing	90°

The two different implementation allowed for this acquisition mode are SMART (only for defence purposes) and the Enhanced SpotLight.

In Enhanced SpotLight the extension in azimuth direction is achieved by a antenna electronic steering scheme requiring the center of the beam steering to be located beyond the center of the imaged spot, thus increasing the observed Doppler bandwidth for each target.

The extension of the frame is about 11 Km $\times$ 11 Km, in azimuth and range direction respectively, the ground resolution is about 1 m $\times$ 1 m.

- **Stripmap Mode:** it is the most common imaging mode, obtained by pointing the antenna along a fixed direction orthogonal to the orbit. The antenna footprint covers a strip on the illuminated surfaces as the platform moves and the system operates. The acquisition is virtually unlimited in the azimuth direction, except for the limitations deriving from the SAR instrument duty cycle (about 600 s, allowing a strip length of 4500 km).

  Two different implementation of this mode are provided: the Himage and the PingPong.

  The Himage is characterized by a swath width of about 40 km and, an azimuth extension for the standard product (square frame) of about 40 Km (corresponding to an acquisition of about 6.5 s); ground resolution is about 3 m $\times$ 3 m.

  In the PingPong mode the acquisition is performed in strip mode alternating the signal polarization between two of possible ones, i.e. VV, HH, HV and

VH. In this polarimetric burst mode only a part of the synthetic antenna length is available in azimuth and consequently the azimuth resolution is reduced. This mode is characterized by a swath width value of about 30 km and an azimuth extension for the standard product of about 30 Km (square frame) corresponding to an acquisition of about 5.0 s; ground resolution is about 15 m $\times$ 15 m.

- **ScanSAR Mode:** it allows larger swath in range with respect to the Stripmap one, but with a less spatial resolution, obtained by periodically stepping the antenna beam to neighbouring sub-swaths. Since only a part of the synthetic antenna length is available in azimuth, the azimuth resolution is hence reduced. In such configuration the acquisition is performed in adjacent strip mode, hence it is virtually unlimited in the azimuth direction, actually it is about 600 s due to the limitations deriving from the SAR instrument duty cycle.

  The two different implementation are allowed for this acquisition mode are WideRegion and HugeRegion, with a spatial resolution selectable from 30 m $\times$ 30 m to 100 m $\times$ 100 m.

  In the WideRegion mode the swath extension in range direction is about 100 Km, corresponding to three adjacent subswaths. The azimuth extension for the standard product is about 100 Km (hence envisaged for the origination of a square frame) corresponding to an acquisition of about 15.0 s.

  In the HugeRegion mode the grouping acquisition over up to six adjacent subswaths allows achieving ground coverage of about 200 Km in the range direction. The azimuth extension for the standard product is about 200 Km (hence envisaged for the origination of a square frame) corresponding to an acquisition of about 30.0 s.

The COSMO-SkyMed products for civil users are divided in Standard and Higher level products [44].

The SAR Standard products are the basic image products of the system, classified in many levels of processing, coded as follows:

- **Level 0 RAW data:** this data consists of time ordered echo data, obtained after decryption and decompression and after applying internal calibration and error compensation; it includes all the auxiliary data required to produce the other basic and intermediate products

- **Level 1A, Single-look Complex Slant (SCS) product:** RAW data focused in slant range and zero Doppler projection, that is the sensor natural acquisition projection; product contains In-Phase and Quadrature of the focused data, weighted and radiometrically equalized

- **Level 1B, Detected Ground Multi-look (DGM) product:** obtained detecting, multi-looking and projecting the Single-look Complex Slant data onto a grid regular in ground (note that SpotLight Mode products are not multi-looked)

- **Level 1C/1D, Geocoded product GEC (1C Level product) and GTC (1D Level product:)** obtained projecting the 1A product onto a regular grid in a chosen cartographic reference system. In case of Lev 1C the surface is the Earth ellipsoid while for the Lev 1D a DEM (Digital Elevation Model) is used to approximate the real Earth surface. In Lev 1D data is constituted by the Backscattering coefficient of the observed scene, multi-looked (except for SpotLight Mode), including the annexed the Incidence Angles Mask

The SAR Higher Level products, suited for mid or even high level remote sensing applications, are composed by the following products:

- **Quicklook:** reduced spatial resolution image for browsing purposes

- **Co-registered products:** a set of image layers coregistered together (i.e. merged in vertical direction), for interferometry, change detection and so on

- **Mosaiked products:** a set of image joined together (i.e. merged in horizontal direction), for large spatial coverage representation

- **Speckle filtered image:** an image with an increased equivalent number of looks (ENL), obtained through various filters available (more details in [44])

- **Interferometric products:** interferometric coherence and phase, in support of the interferometric applications

- **DEM products:** digital elevation data and related height error map obtained with interferometric techniques

The data packaging organization adopted as distribution format for the civilian standard products is HDF5.

6.2 TerraSAR-X

TerraSAR-X is a German mission, it is a Public Private Partnership (PPP) between the German Ministry of Education and Science (BMBF) represented

through the German Aerospace Centre (DLR) and Europe's leading space company, EADS Astrium GmbH.

In the first stage a unique satellite was launched in June 2007, with a scheduled lifetime of 5 years; its design is based on well-founded technology and knowledge achieved during the successful Synthetic Aperture Radar SIR-C/X-SAR and SRTM missions.

It carries a high frequency X-band SAR sensor which can be operated in flexible imaging modes in order to meet the requirements of versatile applications.

It is very similar to its Italian competitor COSMO-SkyMed, without offering a satellite constellation however, and it can acquire imagery in several operational mode:

- **SpotLight (SL):** it an imaging modes that use phased array beam steering in azimuth direction to increase the illumination time, i.e. the size of the synthetic aperture. This leads to a restriction in the image/scene size. Two kinds of scene size are available: 10 km × 10 km for the SpotLight mode with 2 m resolution and 10 km × 5 km (width × length) in the HighResolution SpotLight (HS) mode with 1 m resolution.

- **StripMap (SM):** it is the basic SAR imaging mode, in which the ground swath is illuminated with continuous sequence of pulses while the antenna beam is fixed in elevation and azimuth. This results in an image strip with a continuous image quality (in flight direction).

  In StripMap mode, a spatial resolution of up to 3 m can be achieved. The standard scene size is 30 km × 50 m in order to obtain manageable image files; however, acquisition length is extendable up to 1,650 km.

- **ScanSAR (SC):** in this acquisition mode, electronic antenna elevation steering is used to acquire adjacent, slightly overlapping coverages with different incidence angles that are processed into one scene. In ScanSAR mode, a swath width of 100 km (and even more) will be achieved by scanning four adjacent ground sub-swaths with quasi-simultaneous beams, each with different incidence angle. Due to the switching between the beams, only bursts of SAR echoes are received, resulting in a reduced bandwidth and hence, reduced azimuth resolution.

  In the ScanSAR mode a spatial resolution of up to 18 m is achieved. The standard scene size is 100 km × 150 km (width × length) for easily manageable image files, but again, the acquisition length is extendable up to 1,650 km.

Moreover TerraSAR-X can operate in "Standard TerraSAR-X operational mode", with a single receive antenna mode, that uses a chirp bandwidth of up

Figure 6.2: TerraSAR-X satellite by DLR

to 300 MHz, and in "Advanced imaging mode", where a dual receive antenna is used.

The Basic Image Products of TerraSAR-X are [45]:

- **Slant Range Product in SSC:** The slant range product is a single-look product of the focused radar signal in Single Look Slant Range Complex (SSC). The pixels are spaced equidistant in azimuth (according to the pulse repetition interval PRI=1/PRF) and in slant range (according to the range sampling frequency).

  The data are represented as complex numbers containing amplitude and phase information. Each image pixel is processed to zero Doppler coordinates in range direction, i.e. perpendicular to the flight track.

- **Multi-look Ground Range Detected - MGD:** This product is a detected multi look product with reduced speckle and approximately square resolution cells, with reduced spatial resolution. The image coordinates are oriented along flight direction and along ground range. The pixel spacing is equidistant in azimuth and in ground range.

- **Geocoded Ellipsoid Corrected - GEC:** The GEC is a multi-look detected product, which is resampled and projected to the WGS84 reference ellipsoid assuming one average height. The image is represented in map geometry with ellipsoidal corrections only, thus no terrain correction is performed. Available grid formats are UTM (Universal Transversal Mercator) and UPS (Universal Polar Stereographic). Since the ellipsoid correction does not use height information from a Digital Elevation Model (DEM) for geometric correction, the pixel location accuracy varies depending on the local terrain.

- **Enhanced Ellipsoid Corrected - EEC:** The EEC is a multi-look detected product as well, projected and resampled to the WGS84 reference ellipsoid. However, image distortions caused by varying terrain height are corrected using an external Digital Elevation Model (DEM) available at the payload ground segment (PGS), as SRTM global DSM [45]. The image is represented in map geometry with terrain correction. The available map projections are UTM or UPS. The pixel localization of this product is of a higher accuracy, however, it depends on the type of terrain, the quality and the resolution of the DEM used for the orthorectification, and the incidence angle of the acquisition.

As Enhanced Image Products TerraSAR-X offers:

- **Orthorectified Image - ORISAR:** a highly accurate geocoded image with terrain correction included

- **Radiometrically Corrected Image - RaNSAR:** the products has an additional radiometric calibration or radiometric normalisation

- **Mosaic - MCSAR:** in order to cover a geographical area larger than a standard scene, neighbouring geocoded or orthorectified images are combined into one image in a seamless way

- **Ascending/Descending Merge - ADMSAR:** the ADMSAR product is an orbit merge, i.e. a combination of SAR images from ascending and descending right looking orbits is used for image analysis

In June 2010 a "twin" of TerraSAR-x was launched, the satellite TanDEM-X (TerraSAR-X Add-On for Digital Elevation Measurement). It is a radar satellite almost identical to TerraSAR-X, that circles the Earth together with TerraSAR-X as a unique satellite formation.

They are at only a few hundred meters and they record data synchronously in the so-called StripMap Mode (3 m ground resolution) and thus acquire the data basis for a intereferometric global Digital Elevation Model (DEM) of an unprecedented quality, accuracy, and coverage, since coherence problems are totally solved by the almost contemporary acquisition of the two images used to form the interferogram.

The goal of this mission is to have a homogeneous elevation model available for the Earth's complete land surface in 2014. The expected vertical accuracy is of 2 m (relative) and 10 m (absolute), within a horizontal raster of approximately 12 m $\times$ 12 m, slightly varying depending on the geographic latitude.

Table 6.2: COSMO-SkyMed images features

Area	Acquisition date	Mean incidence angle (deg)	Orbit	Look side
Maussane	13/07/2008	35.7	Asc	Right
Maussane	14/07/2008	55.4	Asc	Right
Merano	30/11/2009	25.9	Desc	Right
Merano	02/12/2009	42.3	Desc	Right

6.3 Data set

The available data for the experimentation are COSMO-SkyMed and TerraSAR-X SpotLight imagery.

As regards COSMO-SkyMed, we have two images forming a stereo pair over the area of Maussane (Southern France) and two images over the area of Merano (Northern Italy) (Figures 6.3 and 6.5). All images belong to the Level 1A (SCS) category products, that is focused data in complex format, in slant range and zero-Doppler projection (images features in Table 6.2).

The two scenes of Maussane were acquired by the same COSMO-SkyMed satellite (CSK1) with incidence angles of 35.7 and 55.4 degrees respectively along an ascending orbit, forming a same-side configuration stereo pair, with a base-to-height ratio equal to 0.7.

The two scenes of Merano were acquired by two different COSMO-SkyMed satellites (CSK1 and CSK2), with incidence angles of 25.9 and 42.3 degrees respectively along an descending orbit, again forming a same-side configuration stereo pair, with a base-to-height ratio equal to 0.3.

The area covered by both stereo pairs is approximately 10 Km $\times$ 10 Km.

The stereo pair orientation of Maussane is based on 25 Ground Points (GPs), used both as GCPs and CPs: 2 GPs have been surveyed by GPS, whereas the remaining 23 GPs have been derived with photogrammetric procedure, from a Cartosat-1 stereo pair, acquired in the framework of the ISPRS-ISRO Cartosat-1 Scientific Assessment Programme (C-SAP) [46], achieving a horizontal and vertical accuracy of about 3 m and 4 m respectively (Figure 6.4).

It has to be underlined that the accuracy is rather poor but also the accuracy of the identification of GPs on the imagery is at the level of 2-3 pixels (if not even worst), since it is much more difficult than for optical imagery due to speckle. Overall, the ground and image coordinate accuracy of GPs is roughly at the same level.

The stereo pair orientation of Merano is based on 20 Ground Points (GPs), used both as GCPs and CPs too; horizontal coordinates are derived from cartography (scale 1:5000) whereas the heights come from a LIDAR Digital Terrain Model (mean elevation accuracy of 0.25 m); both these data are free available on the website of the "Provincia Autonoma di Bolzano" (http://www.provincia.bz.it-/urbanistica/cartografia/cartografia.asp) (Figure 6.6).

Figure 6.3: Maussane COSMO-SkyMed image

As regards TerraSAR-X, we have three images acquired over the town of Hannover (Northern Germany) (Figures 6.7); all images are HighResolution SpotLight (HS) products with extension of 10 Km $\times$ 5 Km (features in Table 6.3). Two images were acquired along an ascending orbit, one of these along a descending orbit. It is possible to choose various combination of images in order to form different stereo pairs; we selected a same-side stereo pair (composed by the first and the second images) with a base-to-height ratio equal to 0.15 and an opposite-side stereo pair (composed by the first and the third images) with a base-to-height ratio equal to 1.

On the Hannover images 20 GPs were been selected, whose coordinates were been derived from a LIDAR DSM, available only on a limited area of the images. In this sense the GPs distribution is not optimal in respect to the orientation of the whole images, and the accuracy results have to be considered reliable only in the GPs area (Figure 6.8).

These data have been provided in the framework of the international project

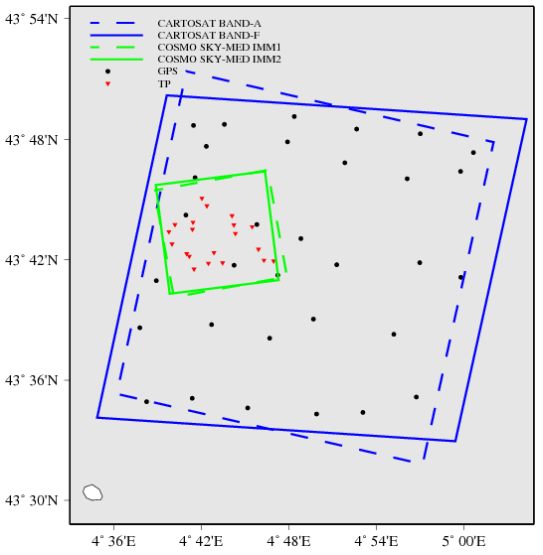

Figure 6.4: GPs distribution on Maussane COSMO-SkyMed image

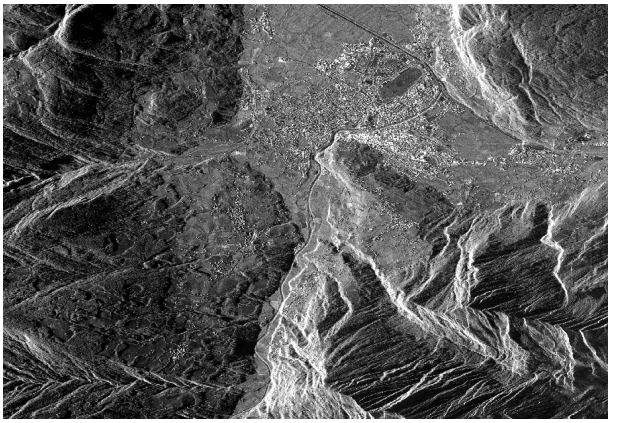

Figure 6.5: Merano COSMO-SkyMed image

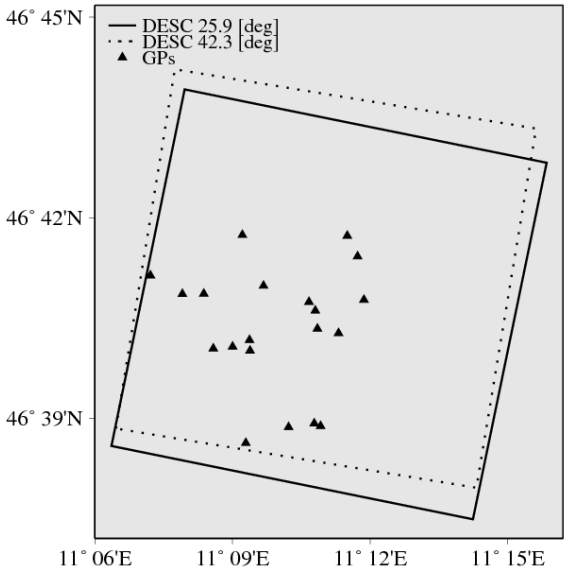

Figure 6.6: GPs distribution on Merano COSMO-SkyMed images

Figure 6.7: Hannover TerraSAR-X image

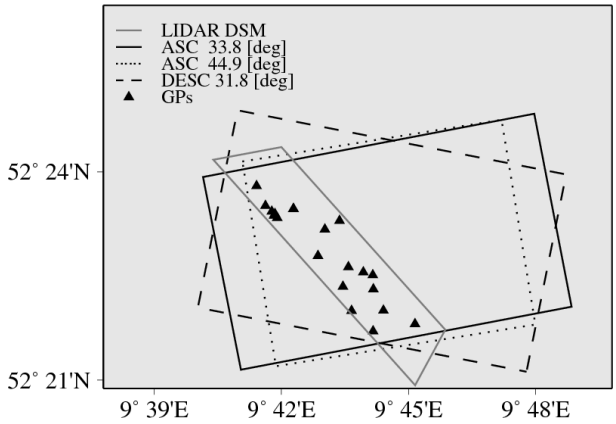

Figure 6.8: GPs distribution on Hannover TerraSAR-X images

Table 6.3: TerraSAR-X images features

Area	Acquisition date	Mean incidence angle (deg)	Orbit	Look side
Hannover	05/12/2007	33.8	Asc	Right
Hannover	10/12/2007	44.9	Asc	Right
Hannover	29/12/2007	31.8	Desc	Right

"Evaluation of DEM derived from TerraSAR-X data", organized by the current ISPRS (International Society for Photogrammetry and Remote Sensing) Working Group VII/2 "SAR Interferometry".

In the Figure 6.9 the difference between a SAR image and an aerial optical image is shown. The interpretation of a SAR image needs of experience and understanding of radar phenomena, as the typical deformations as foreshortening, layover (see Figure 6.10) or shadowing (see Section 3.2).

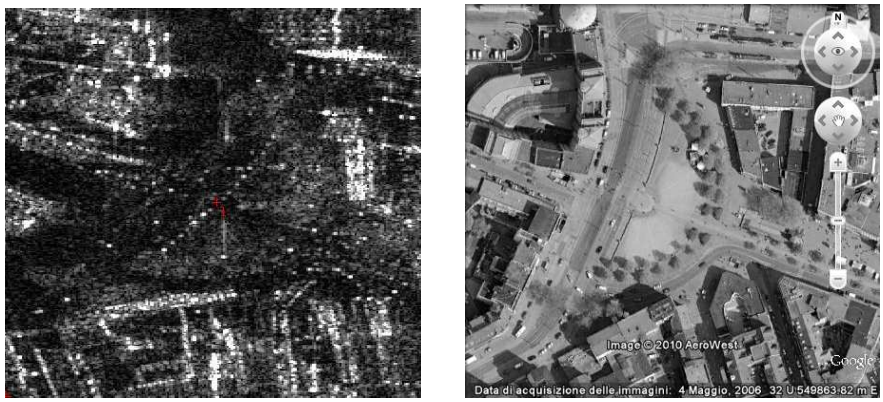

(a) (b)

Figure 6.9: Example of a Ground Point in the center of a square on a TerraSAR-X SAR image (a) and on an optical aerial image (b)

Further additional problems came out for the GPs identification on the opposite-side stereo pair. In fact, only 13 GPs are visible on both images, since the areas illuminated on the first image are in the shadow on the second one. As shown in Figure 6.11, the two images, acquired on opposite-side looking, are significantly different. The GPs useful in this case are in open area, non occluded, visible and well illuminated by the satellite on both look sides.

6.4 Accuracy results of radargrammetric model

To test the effectiveness of the new rigorous model implemented in the software SISAR, the stereo pairs have been orientated varying the number of GCPs and the model accuracy is analyzed, evaluating the RMSE computed over CPs residuals (RMSE CPs), following the standard Hold-Out Validation procedure for accuracy assessment.

(a) (b)

Figure 6.10: Example of layover on a high building on TerraSAR-X SAR image (a) and the same building on an optical aerial image (b)

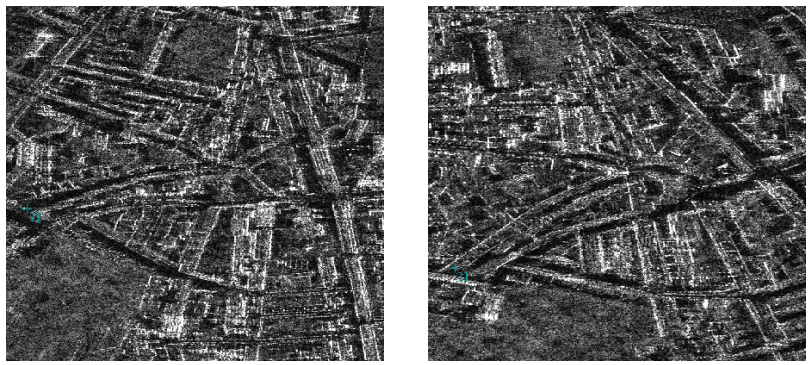

(a) (b)

Figure 6.11: Same area on the ascending TerraSAR-X images (a) and on the descending one (b)

In order to obtain significant results from the statistical point of view, for a given number of GCPs different tests were carried out, using independent sets of GCPs selected under the condition of a homogeneous distribution over the areas covered by the stereo pairs. In the Figure 6.12 an example of 4 different independent sets of 5 GCPs on Hannover test site is shown.

Moreover, SISAR results are compared with those achieved by the rigorous

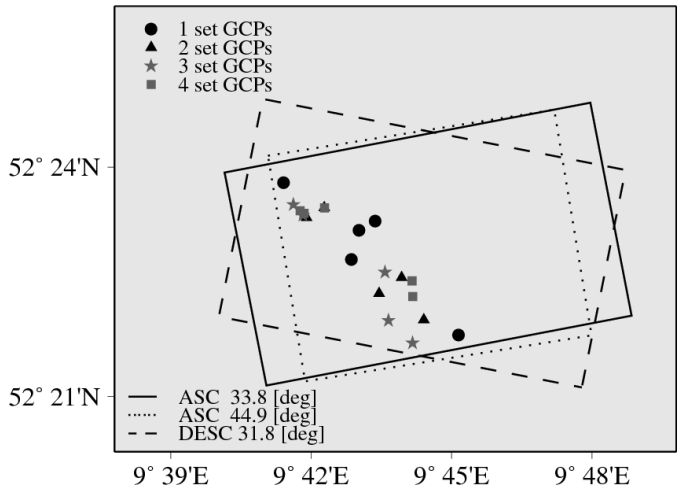

Figure 6.12: Example of 4 different independent sets of 5 GCPs

model implemented in the well known commercial software OrthoEngine v.10.3 (PCI Geomatica).

6.4.1 COSMO-SkyMed imagery results

For Maussane stereo pair, the horizontal and vertical accuracy are both at level of 4.0 - 5.0 m, basically at the same accuracy of the GPs, if the error due to their identification on the COSMO-SkyMed images is also considered togheter with their accuracy on the ground. In Table 6.4 the accuracy is evaluated in terms of RMSE on CPs residuals, and the average, the median and the standard deviation of the RMSE obtained in the several tests carried out using independent sets of GCPs are shown. As regards the model performance varying the independent sets of GCPs, the software shows a stable behavior and the increase of GCPs number does not improve the results remarkably. In this respect, no more than 12 GCPs were considered, also because the number of the CPs would have been too small resulting in a meaningless RMSE CPs. In Figure 6.13 the RMSE CPs histograms for 4 independent sets of 6 GCPs in the case of Maussane are presented; again, it is evident the stability of the model varying the GCPs distribution.

For Merano stereo pair, the horizontal accuracy is at level of 3.0 - 4.0 m, and the vertical one is better than 3.0 m (Table 6.5); no more than 9 GCPs were considered, again to avoid to lower too much the number of the CPs. Also in this

Table 6.4: Results of the scientific software SISAR for the Maussane stereo pair (COSMO-SkyMed)

RMSE CPs Maussane COSMO-SkyMed				
average [m]				
# GCPs	# INDEP. SETs	NORTH	EAST	UP
3	8	4.78	4.51	4.26
6	4	4.32	4.14	3.97
9	2	4.12	4.00	3.94
12	2	4.40	4.03	4.02
median [m]				
# GCPs	# INDEP. SETs	NORTH	EAST	UP
3	8	4.85	4.41	4.31
6	4	4.41	4.10	4.01
9	2	4.12	4.00	3.94
12	2	4.40	4.03	4.02
standard deviation [m]				
# GCPs	# INDEP. SETs	NORTH	EAST	UP
3	8	0.86	0.42	0.21
6	4	0.42	0.19	0.28
9	2	0.53	0.01	0.10
12	2	0.51	0.34	0.13

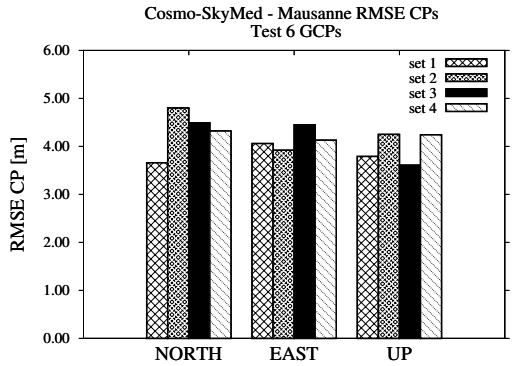

Figure 6.13: RMSE CPs histogram for 4 different independent sets of 6 GCPs for the Maussane stereo pair (COSMO-SkyMed)

Table 6.5: Results of the scientific software SISAR for the Merano stereo pair (COSMO-SkyMed)

RMSE CPs Merano COSMO-SkyMed				
average [m]				
# GCPs	# INDEP. SETs	NORTH	EAST	UP
3	6	2.78	4.14	2.54
6	3	2.55	3.59	2.91
9	2	2.78	3.78	2.70
median [m]				
# GCPs	# INDEP. SETs	NORTH	EAST	UP
3	6	2.81	4.22	2.41
6	3	2.36	3.76	2.67
9	2	2.78	3.78	2.70
standard deviation [m]				
# GCPs	# INDEP. SETs	NORTH	EAST	UP
3	6	0.41	0.30	0.23
6	3	0.27	0.24	0.38
9	2	0.17	0.01	0.19

case, where the GPs accuracy is better, the increase of GCPs number does not improve the results. In Figure 6.14 the RMSE CPs histograms for 3 independent sets of 6 GCPs in the case of Merano are presented.

Finally, just the best results obtained using the commercial software OrthoEngine v. 10.3 (PCI Geomatica), in which the model developed by T. Toutin is embedded, are presented in the Table 6.6. Only tests with 9 GCPs for Merano stereo pair and 9, 12 GCPs for Maussane stereo pair are displayed, since the OrthoEngine v. 10.3 is able to orientate the SAR image with radargrammetric model using 8 GCPs at minimum [47].

The results obtained increasing the GCPs number for Merano and Maussane stereo pairs respectively are not significant due to the low number of CPs.

It is clear that both software basically achieve the same accuracy, but the software OrthoEngine needs 8 GCPs at least for the orientation of SAR images, whereas SISAR gets good results also using few points (3 or 5 GCPs).

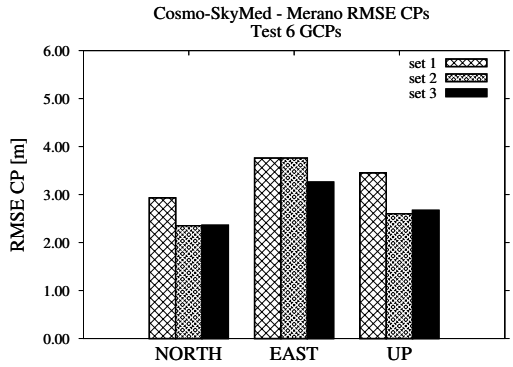

Figure 6.14: RMSE CPs histogram for 3 different independent sets of 6 GCPs for the Merano stereo pair (COSMO-SkyMed)

Table 6.6: Results of the commercial software OrthoEngine v. 10.3 for Maussane and Merano stereo pairs (COSMO-SkyMed)

OrthoEngine Maussane RMSE CPs [m]			
# GCPs	NORTH	EAST	UP
9	5.40	7.03	4.30
12	5.92	6.36	4.23
OrthoEngine Merano RMSE CPs [m]			
# GCPs	NORTH	EAST	UP
9	2.21	3.40	3.23

Table 6.7: Results of the scientific software SISAR for the Hannover same-side stereo pair (TerraSAR-X)

RMSE CPs Hannover same-side TerraSAR-X				
average [m]				
# GCPs	# INDEP. SETs	NORTH	EAST	UP
3	6	2.71	2.84	3.49
5	4	2.38	2.86	3.11
9	2	2.17	2.52	2.98
median [m]				
# GCPs	# INDEP. SETs	NORTH	EAST	UP
3	6	2.7	2.76	3.44
5	4	2.49	2.85	3.18
9	2	2.17	2.52	2.98
standard deviation [m]				
# GCPs	# INDEP. SETs	NORTH	EAST	UP
3	6	0.55	0.35	0.42
5	4	0.34	0.25	0.19
9	2	0.00	0.20	0.24

6.4.2 TerraSAR-X imagery results

As regards the TerraSAR-X data, we have a same-side and an opposite-side stereo pair.

In Table 6.7 the accuracy level achieved in the orientation tests with Hannover same-side stereo pair are presented. The horizontal and vertical accuracy are both at level of 2.5 - 3.5 m (Table 6.4). As regards the model performance achievable varying the independent sets of GCPs, again the software shows a stable behavior and the increase of GCPs number does not improve the results remarkably. In Figure 6.15 the RMSE CPs histograms for 4 independent sets of 5 GCPs in the case of Hannover are presented; again, it is evident the stability of the model varying the GCPs distribution.

The results obtained using the commercial software OrthoEngine v.10.3 (PCI Geomatica), are presented in the Table 6.8; no more than 9 GCPs were considered, for the same reason as before; the height accuracy is slightly worse than SISAR one.

Finally the results of the orientation of the opposite-side stereo pair with SISAR software are presented in Table 6.9. This stereo pair was not oriented

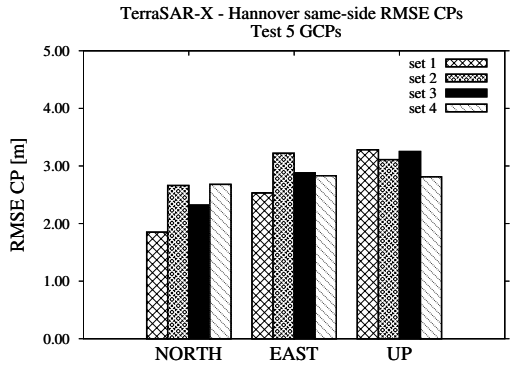

Figure 6.15: RMSE CPs histogram for 4 different independent sets of 5 GCPs for the Hannover same side stereo pair (TerraSAR-X)

Table 6.8: Results of OrthoEngine v. 10.3 for the Hannover same-side stereo pair (TerraSAR-X)

OrthoEngine Hannover same-side RMSE CPs [m]			
# GCPs	NORTH	EAST	UP
9	2.48	2.71	6.39

Table 6.9: Results of the scientific software SISAR for the Hannover opposite-side stereo pair (TerraSAR-X)

RMSE CPs Hannover opposite-side TerraSAR-X				
average [m]				
# GCPs	# INDEP. SETs	NORTH	EAST	UP
3	3	1.97	2.59	3.08
6	2	2.04	2.88	3.06
median [m]				
# GCPs	# INDEP. SETs	NORTH	EAST	UP
3	3	1.94	2.63	2.84
6	2	2.04	2.88	3.06
standard deviation [m]				
# GCPs	# INDEP. SETs	NORTH	EAST	UP
3	3	0.11	0.32	0.38
6	2	0.17	0.29	0.31

with OrthoEngine because too few GPs are available (only 13), so that, again the RMSE CPs cannot be computed reliably.

With this configuration the accuracy is at the same level as a same-side configuration. In Figure 6.16 the RMSE CPs histograms for 3 independent sets of 3 GCPs in the case of Hannover are presented.

6.5 Accuracy results of RPCs model

In this section the results of RPCs generation and their application for COSMO-SkyMed images are presented. As regard RPCs generation, instead of 78 coefficients generally employed in a third order rational polynomial function, a much lower number of coefficients (about 20) are estimated, avoiding the overparametrization and selecting only the estimable and significant parameters as mentioned before.

The generated RPCs were used in order to orientate the stereo pairs; results of RPCs applications are presented in Tables 6.10, 6.11, 6.12 and 6.13 (compare with Tables 6.4, 6.5, 6.7, 6.9 respectively) for all the available stereo pairs.

The RPCs generation, and the corresponding application, has been made using the GCPs independent sets as previously explained for the rigorous model. The accuracy level is just close to the radargrammetric rigorous model one, what

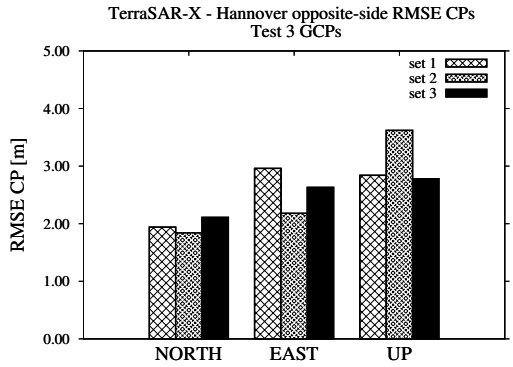

Figure 6.16: RMSE CPs histogram for 4 different independent sets of 5 GCPs for the Hannover opposite-side stereo pair (TerraSAR-X)

Table 6.10: Results of RPC generation and application with different sets of GCPs for the Maussane stereo pair (COSMO-SkyMed)

RMSE CPs Maussane COSMO-SkyMed				
average [m]				
# GCPs	# INDEP. SETs	NORTH	EAST	UP
3	6	5.07	4.59	4.26
6	3	4.49	4.22	3.88
9	2	4.22	4.06	3.78
12	2	4.31	3.90	3.96
median [m]				
# GCPs	# INDEP. SETs	NORTH	EAST	UP
3	6	5.17	4.49	4.23
6	3	4.63	4.16	3.90
9	2	4.22	4.06	3.78
12	2	4.31	3.90	3.96
standard deviation [m]				
# GCPs	# INDEP. SETs	NORTH	EAST	UP
3	6	0.87	0.36	0.28
6	3	0.27	0.21	0.24
9	2	0.49	0.02	0.05
12	2	0.23	0.13	0.06

Table 6.11: Results of RPC generation and application with different sets of GCPs for the Merano stereo pair (COSMO-SkyMed)

RMSE CPs Merano COSMO-SkyMed				
average [m]				
# GCPs	# INDEP. SETs	NORTH	EAST	UP
3	6	2.79	4.23	2.63
6	3	2.58	3.62	2.67
9	2	2.79	3.77	2.71
median [m]				
# GCPs	# INDEP. SETs	NORTH	EAST	UP
3	6	2.72	4.09	2.61
6	3	2.33	3.79	2.42
9	2	2.79	3.77	2.71
standard deviation [m]				
# GCPs	# INDEP. SETs	NORTH	EAST	UP
3	6	0.37	0.49	0.21
6	3	0.46	0.40	0.37
9	2	0.23	0.02	0.02

Table 6.12: Results of RPC generation and application with different sets of GCPs for the Hannover same-side stereo pair (TerraSAR-X)

RMSE CPs Hannover same-side TerraSAR-X				
average [m]				
# GCPs	# INDEP. SETs	NORTH	EAST	UP
3	6	2.41	2.69	3.26
5	4	2.28	2.85	3.07
9	2	2.19	2.46	2.99
median [m]				
# GCPs	# INDEP. SETs	NORTH	EAST	UP
3	6	2.28	2.61	3.12
5	4	2.37	2.72	3.06
9	2	2.19	2.46	2.99
standard deviation [m]				
# GCPs	# INDEP. SETs	NORTH	EAST	UP
3	6	0.39	0.29	0.50
5	4	0.26	0.35	0.13
9	2	0.02	0.04	0.21

Table 6.13: Results of RPC generation and application with different sets of GCPs for the Hannover opposite-side stereo pair (TerraSAR-X)

RMSE CPs Hannover opposite-side TerraSAR-X				
average [m]				
# GCPs	# INDEP. SETs	NORTH	EAST	UP
3	3	1.99	2.76	3.21
6	2	2.09	3.13	2.99
median [m]				
# GCPs	# INDEP. SETs	NORTH	EAST	UP
3	3	1.98	2.45	2.82
6	2	2.09	3.13	2.99
standard deviation [m]				
# GCPs	# INDEP. SETs	NORTH	EAST	UP
3	3	0.12	0.48	0.58
6	2	0.21	0.42	0.36

proves the effectiveness of the RPCs generation tool implemented in SISAR.

The RPCs refinement, as previously mentioned, is not necessary in order to achieve the best accuracy. In fact the SISAR RPCs are calibrated on GCPs and are not affected by biases.

In the Table 6.14 the application of the estimated adjustment parameters are presented for the Hannover same-side stereo pair; RPCs have been applied without any refinement and using 5 GCPs to estimate a shift and an affine adjustment. The adjustment does not improve the results, rather they get slightly worse; this behavior is due to the lack of significance of the adjustment parameters and it worth to be clarified.

In order to check the significance level of the refinement parameters a Student T-test at 5% level has been performed. In Table 6.15 an example of Student T-test is shown for the Hannover same-side stereo pair. All parameters of the affine adjustment are non significant; similar results have been obtained also for the others available stereo pairs. This test confirms the convenience of the SISAR RPCs application without any adjustment.

Table 6.14: Results of the RPCs adjustment for the Hannover same-side stereo pair (TerraSAR-X)

Hannover TerraSAR-X RPCs adjustment results				
Transf.	# GCPs	**RMSE CPs [m]**		
		NORTH	EAST	UP
none	-	1.84	2.58	3.14
shift	5	1.87	2.60	3.15
affine	5	2.10	2.95	3.83

Table 6.15: Significance Student T-test for the RPCs adjustment parameters in the case of the Hannover same-side stereo pair

Hannover same-side stereo pair		
Degrees of freedom		8
$T_{\alpha\ with \alpha=5}$		2.306
Parameter	T_0	Result
$A_0^{(1)}$	0.960	non-significant
$A_1^{(1)}$	0.913	non-significant
$A_2^{(1)}$	0.973	non-significant
$B_0^{(1)}$	1.509	non-significant
$B_1^{(1)}$	1.036	non-significant
$B_2^{(1)}$	1.813	non-significant
$A_0^{(2)}$	1.025	non-significant
$A_1^{(2)}$	0.956	non-significant
$A_2^{(2)}$	1.104	non-significant
$B_0^{(2)}$	1.164	non-significant
$B_1^{(2)}$	0.741	non-significant
$B_2^{(2)}$	1.652	non-significant

Chapter 7

Conclusions

The aim of the work was the development and the implementation of a rigorous radargrammetric model for the orientation of SAR imagery, suited to the Digital Surface Model generation. The model performs a 3D orientation based on two range and two zero-Doppler equations; the results presented are related to the orientation of SAR stereo pairs in slant range and zero-Doppler projection, acquired in SpotLight mode (1 m ground resolution).

The model was defined and implemented in the scientific software SISAR, developed at Geodesy and Geomatic Institute of the University of Rome "La Sapienza".

Moreover a tool for the RPCs generation suited to SAR imagery has been included in SISAR software. RPCs model is a well-known and validated method to orientate optical satellite imagery, representing a standard re-parametrized form of the rigorous sensor model. Its implementation is standard and generalized, it is available in several commercial software, and the performances of the RPCs model can be at the level of the ones from rigorous models.

The model implemented has been tested on COSMO-SkyMed and on Terra-SAR-X images; both satellites are able to acquire imagery in SpotLight mode, representing the most advanced SAR technology actually available.

As regards COSMO-SkyMed, we have two images forming a stereo pair over the area of Maussane (Southern France) and two images over the area of Merano (Northern Italy). All images belongs to the Level 1A (SCS) category products, that are focused data in complex format, in slant range and zero-Doppler projection. The area covered by both stereo pairs is approximately 10 Km x 10

Km.

As regards TerraSAR-X, we have three images acquired over the town of Hannover (Northern Germany), all images are HighResolution SpotLight (HS) products with extension of 10 Km $\times$ 5 Km. Two images were acquired along an ascending orbit, one of these along a descending orbit. It is possible to choose various combination of images in order to form different stereo pairs; we selected a same-side stereo pair and an opposite-side stereo pair.

To test the effectiveness of the new rigorous model implemented in the software SISAR, the stereo pairs have been orientated varying the number of GCPs and the model accuracy is analyzed, evaluating the RMSE computed over CPs residuals (RMSE CPs), following the standard Hold-Out Validation procedure for accuracy assessment. In order to obtain significant results from the statistical point of view, for a given number of GCPs different tests were carried out, using independent sets of GCPs selected under the condition of a homogeneous distribution over the areas covered by the stereo pairs.

Moreover, SISAR results are compared with those stemming from commercial software OrthoEngine v.10.3 (PCI Geomatica).

The accuracy evaluation shows that the vertical accuracy is at level of 4.0 - 5.0 m in the case of Maussane test site and at level of 3.0 m in the case of Merano one; this preliminary results are satisfying, considering the mean accuracy of the available GPs. An investigation using more accurate GPs, for example GPS points, is recommended, although it has to be underlined that also the uncertainty of the GPs collimation on the images (1-3 pixels) could affect the results.

As regards the model performance varying the independent sets of GCPs, the software shows a stable behavior and the increase of GCPs number does not improve the results remarkably.

As for TerraSAR-X data, we have a same-side and an opposite-side stereo pairs over the town of Hannover. The accuracy level achieved in the orientation tests with both stereo configuration is about 2.5 - 3.5 m. Again, the software shows a stable behavior.

The commercial software OrthoEngine provides basically the same level of accuracy of SISAR in the case of Maussane and Merano stereo pair, whereas in the Hannover stereo pair the height accuracy with SISAR software is better than OrthoEngine one; a significant difference between the two software is that OrthoEngine needs 8 GCPs at least for the orientation of SAR images, whereas SISAR gets good results also using few points (3 or 5 GCPs).

The application of RPCs model to SAR stereo pairs gives good results, absolutely comparable with those derived through the radargrammetric rigorous model, what proves the effectiveness of the RPCs generation tool implemented in SISAR.

The results obtained are representative of the geometric potentialities of

SpotLight stereo pairs as regards 3D surface reconstruction. Anyway, it has to be recalled that the accuracy of the DSMs generated by the radargrammetric approach is strictly affected by the quality of the subsequent matching procedure, which is presently a hot topic and will be addressed in the future investigations.

Bibliography

[1] T. Toutin and L. Gray. State-of-the-art of elevation extraction from satellite sar data. *ISPRS Journal of Photogrammtery & Remote Sensing*, 55:13–33, 2000.

[2] T. Toutin. Stereomapping with spot-p and ers-1 sar images. *International Journal of Remote Sensing*, 21(8), 2000.

[3] H. Raggam, K. Gutjahr, R. Perko, and M. Schardt. Assessment of the stereo-radargrammetric mapping potential of terrasar-x multibeam spotlight data. *IEEE Transactions on Geoscience and Remote Sensing*, 48(2), 2010.

[4] T. Toutin and R. Chenier. 3-d radargrammetric modeling of radarsat-2 ultra-fine mode: preliminary results of the geometric calibration. *IEEE Geoscience and Remote Sensing Letters*, 6(2), 2009.

[5] F. W. Leberl. Radargrammetric image processing. *Artec House, Norwood MA*, 1990.

[6] M. Crespi, F. Fratarcangeli, F. Giannone, and F. Pieralice. A new rigorous model for high resolution satellite imagery orientation: application to eros a and quickbird. *International Journal of Remote Sensing (in press)*, 2010.

[7] S. Meric, F. Fayard, and E. Pottier. Radargrammetric sar image processing. *In: Pei-Gee Peter Ho (Eds.), Geoscience and Remote Sensing, Intech*, pages 421–454, 2009.

[8] Z. Li, Q. Zhu, and C. Gold. Digital terrain modeling: principles and methodology. *CRC Press, Florida, USA*, pages 39–51, 2005.

[9] M. Mansourpour, M.A. Rajabi, and J. A. R. Blais. Effects and performance of speckle noise reduction filters on active radar and sar images. *ISPRS Workshop, Topographic Mapping from Space, Ankara (Turkey)*, 2006.

[10] R. Lanari, S.Zoffoli, E. Sansosti, G. Fornaro, and F. Serafino. New approach for hybrid strip-map/spotlight SAR data focusing. *Radar, Sonar and Navigation, IEE Proceedings*, 148:363–372, 2001.

[11] R. F. Hanssen. Radar interferometry data interpretation and error analysis. *Springer*, 2001.

[12] G. La Prade, S.J. Briggs, R.J. Farrell, and E.S. Leonardo. Stereoscopy. *Chapter X of the Manual of Photogrammetry, Fourth Edition, ASP, Falls Church, USA*, 1980.

[13] T. Toutin. Elevation modeling from satellite data. *Encyclopedia of Analytical Chemistry*, 2006.

[14] F. Fayard, S. Meric, and E. Pottier. Matching stereoscopic sar images for radargrammetric applications. *International Geoscience and Remote Sensing Symposium, Barcelona (Spain)*, 2007.

[15] G. La Prade. An Analytical and Experimental Study of Stereo for Radar. *Photogrammetric Engineering*, 29(2):294–300, 1963.

[16] J. D. Wegner, S. Auer, and Uwe Soergel. Extraction and geometrical accuracy of double-bounce lines in high resolution sar images. *Photogrammetric Engineering and Remote Sensing*, 76(9):1071–1080, 2010.

[17] Z. Shi and K.B. Fung. A comparison of digital speckle filters. *Geoscience and Remote Sensing Symposium, 1994. Surface and Atmospheric Remote Sensing: Technologies, Data Analysis and Interpretation*, 4:2129–2133, 1994.

[18] V.S. Frost, J. Stiles, K. Shanmugan, and J. Holtzman. A model for radar images and its application to adaptive digital filtering of multiplicative noise. *IEEE Transaction on Pattern Analysis and Machine Intelligence*, PAMI-4(2):157–166, 1982.

[19] J.S. Lee. Refined filtering of image noise using local statistics. *Computer graphics and Image Processing*, pages 380–389, 1981.

[20] T. Toutin. Generating dem from stereo images with a photogrammetric approach: Examples with vir and sar data. *EARSeL Advances in Remote Sensing*, 4(2), 1995.

[21] T. Toutin. Opposite side ers-i sar stereo mapping over rolling topography. *IEEE Transactions On Geoscience And Remote Sensing*, 34(2), 1996.

[22] T. Toutin. Impact of terrain slope and aspect on radargrammetric dem accuracy. *ISPRS Journal of Photogrammetry and Remote Sensing*, 57, 2002.

[23] T. Toutin. Stereo radarsat for mapping applications. *2nd International ADRO Symposium, Montreal, Canada*, 1998.

[24] T. Toutin. Evaluation of radargrammetric dem from radarsat images in high relief areas. *IEEE Transactions On Geoscience And Remote Sensing*, 38(2), 2000.

[25] M. Crosetto and F. Pérez Aragues. Radargrammetry and sar interferometry for dem generation: validation and data fusion. *Proceedings of CEOS SAR Workshop, ESA-CNES, Toulouse, France*, 1999.

[26] T. Westin. Precision rectification of spot imagery. *Photogrammetric Engineering and Remote Sensing*, 56(2):247–253, 1990.

[27] P.J.G. Teunissen and A. Kleusberg. Gps for geodesy. *Springer-Verlag. ISBN: 3-540-63661-7*, 1998.

[28] B. Hofmann Wellenhof, H. Lichtenegger, and E. Wasle. Gnss global navigation satellite system. *Spinger-Verlag. ISBN: 978-3-211-73012-6*, 2008.

[29] O. Montenbruck and E. Gill. Satellite orbits. *Springer, Berlin*, 2001.

[30] International Earth Rotation and Reference System Service. http://www.iers.org. 2010.

[31] F. Sansò. Il trattamento statistico dei dati. *Editore CLUP, Milano*, 1989.

[32] C.V. Tao and Y. Hu. The rational function model. a tool for processing high resolution imagery. *Earth Observation Magazine*, 10(1):13–16, 2001.

[33] NIMA. The compendium of controlled extensions (ce) for the national imagery transmission format (version 2.1) nitfs technical board. 2000.

[34] C.V. Tao and Y. Hu. 3d reconstruction methods based on the rational function model. *Photogrammetric Engineering & Remote Sensing*, 68(7):705–714, 2002.

[35] H.B. Hanley and C. S. Fraser. Sensor orientation for high-resolution satellite imagery: further insights into bias-compensated rpc. *Proceeding of XX ISPRS Congress, Istanbul, Turkey*, 2004.

[36] C.V. Tao and Y. Hu. A comprehensive study of the rational function model for photogrammetric processing. *Photogrammefric Engineering & Remote Sensing*, 67(12):1347–1357, 2001.

[37] C.V. Tao and Y. Hu. Use of the rational function model for image rectification. *Canadian Journal of Remote Sensing*, 27(6):593–602, 2001.

[38] T. Toutin, R. Chénier, and Y. Carbonneau. 3d models for high resolution images: examples with quickbird, ikonos and eros. *Proceedings of ISPRS Commission IV Symposium, Joint International Symposium on Geospatial Theory, Processing and Applications, Ottawa*, pages 547–551, 2000.

[39] A. Neumaier. Solving ill-conditioned and singular linear systems: a tutorial on regularization. *SIAM Review*, 40(3):636–666, 1998.

[40] M. Crespi, F. Fratarcangeli, F. Giannone, and F. Pieralice. Chapter 4 – overview on models for high resolution satellites imagery orientation. *Geospatial Technology for Earth Observation data, Springer, Heidelberg*, 2009.

[41] M. Bianconi, M. Crespi, F. Fratarcangeli, F. Giannone, and F. Pieralice. A new strategy for rational polynomial coefficients generation. *Proceeding EARSeL Joint Workshop Remote Sensing, New Challenges of High Resolution, Bochum (Germany)*, 2008.

[42] G.H. Golub and C. F. VanLoan. Matrix computation. *The Johns Hopkins University Press, Baltimore and London*, 1993.

[43] Italian Space Agency ASI. Cosmo-skymed system description and user guide. *Available at https://eopi.asi.it*, 2007.

[44] Italian Space Agency ASI. Cosmo-skymed sar products handbook. *Available at https://eopi.asi.it*, 2007.

[45] Infoterra. Terra sar-x services image product guide. *Available at: http://www.infoterra.de/documents*, 2009.

[46] R. Nandakumar, Amitabh, MPT Chamy, S. Soma, S. Kopparthi, G. Paswan, S. Prakash, and S. Singh. Synthesis of investigations under isprs-isro cartosat-1 scientific assessment programme primarily for dsm generation. *The International Archives of the Photogrammetry, Remote Sensing and Spatial Information Sciences, Beijing*, XXXVII, 2008.

[47] PCI Geomatics. Pci geomatica 10.3 user guide. 2009.